

RESEARCH ARTICLE

10.1002/2013JD020046

Key Points:

- Dust absorption has a positive feedback on dust emissions
- Stronger absorption leads to longer range transport of dust aerosols
- Dust forcing impacts are more tied to refractive index than particle shape

Supporting Information:

- Readme
- Supplemental Table S1
- Supplemental Table S2
- Supplemental Table S3
- Supplemental Table S4
- Supplemental Table S5
- Supplemental Table S6
- Supplemental Table S7

Correspondence to:

P. R. Colarco,
Peter.R.Colarco@nasa.gov

Citation:

Colarco, P. R., E. P. Nowottnick, C. A. Randles, B. Yi, P. Yang, K.-M. Kim, J. A. Smith, and C. G. Bardeen (2014), Impact of radiatively interactive dust aerosols in the NASA GEOS-5 climate model: Sensitivity to dust particle shape and refractive index, *J. Geophys. Res. Atmos.*, 119, 753–786, doi:10.1002/2013JD020046.

Received 17 APR 2013

Accepted 10 DEC 2013

Accepted article online 13 DEC 2013

Published online 17 JAN 2014

This is an open access article under the terms of the Creative Commons Attribution-NonCommercial-NoDerivs License, which permits use and distribution in any medium, provided the original work is properly cited, the use is non-commercial and no modifications or adaptations are made.

Impact of radiatively interactive dust aerosols in the NASA GEOS-5 climate model: Sensitivity to dust particle shape and refractive index

Peter R. Colarco¹, Edward P. Nowottnick^{1,2}, Cynthia A. Randles^{1,3}, Bingqi Yi⁴, Ping Yang⁴, Kyu-Myong Kim^{1,3,5}, Jamison A. Smith⁶, and Charles G. Bardeen⁷

¹Atmospheric Chemistry and Dynamics Laboratory, NASA GSFC, Greenbelt, Maryland, USA, ²NASA Postdoctoral Program, NASA GSFC, Greenbelt, Maryland, USA, ³GESTAR/Morgan State University/NASA GSFC, Greenbelt, Maryland, USA,

⁴Department of Atmospheric Sciences, Texas A&M University, College Station, Texas, USA, ⁵Climate and Radiation Laboratory, NASA GSFC, Greenbelt, MD, USA, ⁶Laboratory for Atmospheric and Space Physics, University of Colorado Boulder, Boulder, Colorado, USA, ⁷National Center for Atmospheric Research, Boulder, Colorado, USA

Abstract The radiative effects of Saharan dust aerosols are investigated in the NASA GEOS-5 atmospheric general circulation model. A sectional aerosol microphysics model (CARMA) is run online in GEOS-5. CARMA treats the dust aerosol lifecycle, and its tracers are radiatively coupled to GEOS-5. A series of AMIP-style simulations are performed, in which input dust optical properties (particle shape and refractive index) are varied. Simulated dust distributions for summertime Saharan dust compare well to observations, with best results found when the most absorbing dust optical properties are assumed. Dust absorption leads to a strengthening of the summertime Hadley cell circulation, increased dust lofting to higher altitudes, and a strengthening of the African easterly jet, resulting in increased dust atmospheric lifetime and farther northward and westward transport. We find a positive feedback of dust radiative forcing on emissions, in contrast with previous studies, which we attribute to our having a relatively strong longwave forcing caused by our simulating larger effective particle sizes. This longwave forcing reduces the magnitude of midday net surface cooling relative to other studies, and leads to a nighttime warming that results in higher nighttime wind speeds and dust emissions. The radiative effects of dust particle shape have only minor impact on transport and emissions, with small (~5%) impact on top of atmosphere shortwave forcing, in line with previous studies, but relatively more pronounced effects on shortwave atmospheric heating and surface forcing (~20% increase in atmospheric forcing for spheroids). Shape effects on longwave heating terms are of order ~10%.

1. Introduction

Mineral dust aerosols play many roles in Earth's climate system. Scattering and absorption of shortwave (i.e., solar) and longwave (i.e., thermal) radiation by dust particles directly influence Earth's radiation balance [Sokolik and Toon, 1996; Balkanski et al., 2007]. The indirect effect of dust particles on climate includes their modification of cloud properties. For example, by acting as an additional source of cloud condensation nuclei (CCN), dust particles can lead to smaller cloud droplets, hence limiting droplet coalescence efficiency and suppressing precipitation [Rosenfeld et al., 2001]. The facility of dust particles to act as ice nuclei in clouds offers another pathway toward indirect climate effects, where dust is observationally linked to glaciation in mildly supercooled altocumulus clouds [Sassen et al., 2003]. Dry air layers associated with Saharan dust outbreaks may play a role in suppressing convection and tropical cyclone formation in the Atlantic [Dunion and Velden, 2004; Wong and Dessler, 2005], and satellite observations suggest an inverse relationship between the presence of dust and tropical cyclone activity in the same region [Evan et al., 2006; Lau and Kim, 2007]. Observational evidence from meteorological analyses suggests a role for radiative heating of Saharan dust layers in modulating the amplitude of easterly waves in which the dust is typically transported [Jones et al., 2004]. Biological productivity (i.e., photosynthetic activity in phytoplankton) in many ocean regions is limited by the availability of iron, which has as a major and variable source the deposition of mineral dust aerosols [Martin, 1990; Fung et al., 2000; Mahowald et al., 2009]. To the extent that an enhanced supply of nutrients from dust deposition mitigates the iron stress limitation in these ecosystems, dust can modulate the oceanic uptake of CO₂ at the ocean-air interface [see review in Jickells et al., 2005]. Similarly, dust can be an important nutrient source to terrestrial ecosystems [Swap et al., 1992]. Atmospheric dust aerosols play a role in tropospheric photochemistry pathways by altering photolysis rates and

acting as a surface on which heterogeneous reactions can occur [Dentener *et al.*, 1996; Bian and Zender, 2003; Bauer *et al.*, 2004]. Finally, long-range transport of dust aerosols are a source of fine particulate matter associated with poor air quality episodes [Prospero, 1999] and are a vector for transporting microorganisms associated with coral reef mortality [Shinn *et al.*, 2000].

Because of the importance of mineral dust aerosols in Earth's climate system there has been a considerable effort to model their temporally and spatially varying distributions in chemical transport models and global climate models [Tegen and Fung, 1994; Mahowald *et al.*, 1999; Ginoux *et al.*, 2001; Zender *et al.*, 2003; Colarco *et al.*, 2003; Su and Toon, 2009; Nowottnick *et al.*, 2010]. Synthesis studies of various modeling efforts reveal the importance of dust to the total aerosol loading, but also show wide variability in modeled emissions and atmospheric burden [Zender *et al.*, 2004; Textor *et al.*, 2006; Huneus *et al.*, 2011]. There also remain large differences in the treatment of the particle size distribution and its evolution in dust models that can greatly affect the dust radiative impacts [Kok, 2011]. These issues are convolved with model-dependent factors that impact source, sink, and transport terms in the aerosol evolution (e.g., spatial resolution, dynamical core, turbulent and convective parameterizations, precipitation, etc.).

The direct radiative effects of dust aerosols on Earth's climate thus remain uncertain in both magnitude and even sign in recent assessments [IPCC, 2007]. In addition to the uncertainties in atmospheric burden and particle size distribution noted above, there remains an uncertainty in the dust optical properties themselves. These are manifest in the composition of the dust—generally a function of source and particle size—and these will have important effects on the radiative properties of the aerosol [Sokolik and Toon, 1999; Quijano *et al.*, 2000]. The typical modeling paradigm is to carry the size resolved mass of dust as a number of tracers, and for each tracer to specify optical properties that are a function of size and the spectrally varying complex index of refraction. Often the refractive indices are derived from measurements based on in situ dust samples [e.g., Shettle and Fenn, 1979; Hess *et al.*, 1998]. Optical properties derived from these measurements suggest considerably more shortwave absorption by dust than do properties inferred from space-based remote sensing techniques [Kaufman *et al.*, 2001; Moulin *et al.*, 2001; Colarco *et al.*, 2002; Sinyuk *et al.*, 2003]. Retrievals from Sun photometer observations also suggest very weakly absorbing dust in the shortwave [Kim *et al.*, 2011]. Overall, dust absorption as represented by the imaginary component of the refractive index may vary by an order of magnitude among these various data sets [Balkanski *et al.*, 2007]. With such large uncertainty in the dust refractive index—reflecting differences in mineralogy across source regions, as well as emission and transport processes—the dust radiative properties as treated in chemical transport models are not well constrained (see, for example, Kinne *et al.* [2003], as well as the diversity in dust mass extinction efficiency among the various models shown in Kinne *et al.* [2006] and Huneus *et al.* [2011]).

Additionally, spectral dust optical properties are often derived assuming particle sphericity using Mie theory, although it is well known that dust particles are nonspherical. Shape effects are understood to be important to retrieval of aerosol properties from spectral, angular, and polarized reflectance measurements [e.g., Feng *et al.*, 2009], but the importance to flux calculations like those performed in GCM radiative transfer schemes has been thought to be small [Mishchenko *et al.*, 1995]. Recently, however, improved databases of optical properties for nonspherical dust-like aerosols [e.g., Meng *et al.*, 2010] have been employed in radiative transfer calculations, suggesting uncertainties in top of atmosphere (TOA) fluxes of as much as 30% due to dust shape effects [Yi *et al.*, 2011]. By contrast, Räisänen *et al.* [2012] found in general circulation model simulations including dynamically and radiatively interactive dust aerosols that dust shape effects had a small impact on radiative fluxes and heating rates, hence a generally negligible climate effect due to nonspherical dust optics. The apparent contrast between the Yi *et al.* [2011] and Räisänen *et al.* [2012] conclusions highlights the need for further study of the impact of particle shape on dust aerosol radiative forcing, as each study employed rather different modeling tools and assumptions about the dust particle composition (refractive index) and size and shape distributions.

In this study we investigate the impact of the choice of dust optical properties on the simulation of the dust aerosol lifecycle and the resultant radiative fluxes calculated in the NASA Goddard Earth Observing System (GEOS) atmospheric general circulation model (AGCM). A new sectional aerosol microphysics module is incorporated in the GEOS AGCM that is used to simulate the lifecycle of dust and sea salt aerosols, considering emission, transport, and loss processes. The size resolved aerosol tracers are radiatively coupled and transported dynamically within the AGCM. A number of simulations are conducted in which we vary the

assumed dust optical properties, considering both particle shape and spectrally varying index of refraction. Different aerosol spatial (horizontal and vertical) and particle size distributions result from the various simulations, owing to the different radiative forcing imposed on the model by the choice of dust optical properties and its subsequent effect on the model climate (e.g., temperature and winds). Consistent comparisons of the various simulations are ensured through evaluation first against a number of aerosol observational data sets. These comparisons are made to establish the overall credibility of the new aerosol modeling capability, as well as to characterize how different choices of dust optical properties affect the atmospheric state in the model, and thus the distributions of aerosol simulated. The radiative fluxes due to dust are then explored diagnostically, using fields saved from a benchmark model run, and interactively through the simulations for which the dust aerosols feed back on the model. This work is thus complementary to recent studies exploring the sensitivity of dust radiative fluxes to particle shape [e.g., *Yi et al.*, 2011; *Räisänen et al.*, 2012] but extends upon them by incorporating different sets of dust optical properties. It also lays the groundwork toward developing a treatment of nonspherical dust optical properties in our AGCM suitable for future observation (e.g., lidar, satellite radiance) simulation studies.

In section 2 we describe the model and the dust optical properties used. In section 3 we evaluate our simulations with observational data sets. In section 4 we discuss the impact of the dust optical properties on the climate of the model. We present conclusions in section 5.

2. Model Description

2.1. NASA Goddard Earth Observing System Model, Version 5 (GEOS-5)

The GEOS-5 AGCM is one of the main components of the GEOS-5 atmospheric data assimilation system and Earth system model [*Rienecker et al.*, 2008]. The GEOS-5 system is used to provide (i) research quality atmospheric reanalyses for use by the scientific community (e.g., the Modern-Era Retrospective Analysis for Research and Applications or MERRA [*Rienecker et al.*, 2011]), (ii) forward processed analyses and forecasts for use by NASA instrument teams [e.g., *Zhu and Gelaro*, 2008], and (iii) analyses and forecasts for use in various field campaigns [e.g., *Bian et al.*, 2013]. It has also been used as a tool to study aerosol impacts on weather [e.g., *Reale et al.*, 2011] and climate [e.g., *Ott et al.*, 2010; *Randles et al.*, 2013] by inclusion of an online aerosol module [*Colarco et al.*, 2010].

The GEOS-5 AGCM simulates traditional meteorological parameters (wind, temperature, pressure, etc.), combining the finite volume dynamical core of *Lin* [2004] with a column physics package. Turbulence is based on *Lock et al.* [2000]. Convection is from the relaxed Arakawa-Schubert (RAS) scheme [*Moorthi and Suarez*, 1992] and incorporates a prognostic cloud scheme. Interactions with the land surface are through the catchment model of *Koster et al.* [2000]. Radiative transfer is computed using the parameterization of *Chou and Suarez* [1994, 1999] and *Chou et al.* [2001], incorporating gaseous absorption and scattering and absorption by aerosols in 8 shortwave and 10 longwave bands. The model can be run at various horizontal spatial resolutions. The simulations considered in this study are run at a $2^\circ \times 2.5^\circ$ latitude-by-longitude spatial resolution. There are 72 vertical layers distributed in a hybrid sigma coordinate system that is terrain following near the surface and transforming to pressure coordinates near 180 hPa with the model top at 1 Pa (~ 85 km).

We note that an integrated ocean circulation model was not yet available in GEOS-5 when this study was performed. Sea surface temperatures are thus prescribed and do not respond to dust radiative forcing. Consequently, the results presented below must be viewed somewhat tentatively as the model climate may respond quite differently when a coupled ocean is considered.

2.2. Community Aerosol and Radiation Model for Atmospheres (CARMA)

We have coupled the Community Aerosol and Radiation Model for Atmospheres (CARMA) [*Toon et al.*, 1988; *Jensen et al.*, 1994; *Ackerman et al.*, 1995] to GEOS-5. CARMA is a sectional aerosol and cloud microphysics model that has been applied to simulate dust [*Colarco et al.*, 2002, 2003; *Su and Toon*, 2009], sea salt [*Madry et al.*, 2011; *Fan and Toon*, 2011], sulfate [*English et al.*, 2011, 2012], and carbonaceous aerosols [*Colarco et al.*, 2004; *Matichuk et al.*, 2007, 2008]. Although the mechanisms in CARMA permit treatment of aerosol growth and nucleation, our setup of CARMA in this study is simple. For dust, we partition the aerosol mass across eight logarithmically spaced size bins spanning radius from 0.1–10 μm . This setup is the same as in *Colarco et al.* [2003].

Table 1. Summary of Experiments and Characteristics

Experiment Name	Refractive Index	Shape	AOT ₅₅₀	SSA ₅₅₀	g ₅₅₀
No Forcing ^a	OPAC ^b	Spheres	1.00	0.86	0.75
OPAC-Spheres	OPAC	Spheres	1.00	0.86	0.75
OPAC-Spheroids	OPAC	Spheroids ^e	1.26	0.88	0.77
OPAC-Ellipsoids	OPAC	Ellipsoids ^f	1.27	0.88	0.77
SF-Spheres	Shettle and Fenn ^c	Spheres	1.00	0.82	0.76
SF-Ellipsoids	Shettle and Fenn	Ellipsoids	1.24	0.84	0.78
OBS-Spheres	Colarco/Kim and Shettle and Fenn ^d	Spheres	0.98	0.93	0.74
OBS-Spheroids	Colarco/Kim and Shettle and Fenn	Spheroids	1.22	0.92	0.75

^aIn the “No Forcing” run the aerosols are passive tracers. Here the optical properties refer to those which are used to compute the diagnostic aerosol optical thickness.

^bOPAC refers to dust refractive indices from *Hess et al.* [1998].

^cShettle and Fenn refers to dust refractive indices from *Shettle and Fenn* [1979].

^dColarco/Kim and Shettle and Fenn refers to dust refractive indices merged from *Colarco et al.* [2002] and *Kim et al.* [2011] in the UV/visible and fit by a log-power law curve to merge with the *Shettle and Fenn* [1979] values in the infrared.

^eThe spheroidal shape distribution is from *Dubovik et al.* [2006].

^fThe ellipsoidal shape distribution is from *Yi et al.* [2011].

The dust tracers are radiatively coupled to the host model through the GEOS-5 native radiative transfer interface. The only CARMA-based microphysical process affecting the dust tracers is sedimentation. For purposes of tracking the aerosol mass, we assume that the dust particles are homogeneous spheres with a density of 2650 kg m^{-3} , and the sedimentation velocity is computed accordingly for the effective radius of the particular size bin. We do not consider the effects of particle nonsphericity on particle fall speed, as has been done in other studies [e.g., *Colarco et al.*, 2003; *Ginoux*, 2003]. Other processes relating to emissions and deposition are described below. Sea-salt aerosols are incorporated in a similar fashion (section 2.5). There is no interaction of the dust and sea salt. The aerosol microphysics module is not coupled to the model hydrological cycle, and so we do not consider the aerosol indirect effect in this study.

2.3. Dust Emission and Removal Processes

Dust emission and removal processes essentially follow from *Colarco et al.* [2003] and *Colarco et al.* [2010]. Dust emissions are based on *Ginoux et al.* [2001], who provide a map of potential dust source locations based on the observed correlation of dust emitting regions with large-scale topographic depressions. In this study the topographic map is updated and provided at a $1^\circ \times 1^\circ$ latitude-by-longitude spatial resolution (P. Ginoux, personal communication). Dust emissions are computed at each model time step and grid box as

$$E_{i,j} = s_r \cdot C \cdot S_{i,j} \cdot u_{i,j}^2 (u_{i,j} - u_t); u_{i,j} > u_t \quad (1)$$

where $S_{i,j}$ is the grid box i,j potential efficiency to act as a dust source (dimensionless with a value 0–1 in magnitude) and $u_{i,j}$ is the model wind speed at 10 m altitude. Note that the source function $S_{i,j}$ has been conservatively remapped to the $2^\circ \times 2.5^\circ$ latitude-by-longitude spatial resolution of the AGCM wind fields. u_t is the particle size-dependent threshold wind speed that must be exceeded in order to emit dust [*Martcorena and Bergametti*, 1995]. This threshold wind speed is increased for wet soils following *Ginoux et al.* [2001]. s_r is the relative fraction of dust particles existing in the soil at each of our size bins, similar to *Colarco et al.* [2003]. We assume a globally constant distribution for silt-sized particles ($1 \mu\text{m} < \text{radius} < 10 \mu\text{m}$), so $s_r = 0.25$ for each of the four size bins in that range. We assume that the mass of clay-sized particles (radius $< 1 \mu\text{m}$) is 10% of the silt mass, and the relative partitioning of the four submicron size bins follows from [*Tegen and Lacis*, 1996, their Table 1]. C is a global tuning constant used to set the overall emissions. In practical terms, since there are no global observations of dust emissions, C is tuned to give a reasonable dust loading or dust aerosol optical thickness and is thus model dependent. In all the experiments described in this study we set $C = 0.35 \mu\text{g s}^{-2} \text{m}^{-5}$.

Once emitted, dust is transported by advection, as well as turbulent and convective mixing. Dust is removed by sedimentation (calculated in the CARMA module), or else by turbulent dry deposition and large-scale and convective-scale wet removal. The sedimentation fall speed is computed for each size bin following the formulation for Stokes' law and accounting for noncontinuum effects at low Reynold's number flow (i.e., low air density or small particle sizes) after *Pruppacher and Klett* [1997]. This formulation assumes spherical particle shapes. We have neglected consideration of particle nonsphericity on this term, which would have the

effect of reducing the fall speed [see, e.g., Colarco *et al.*, 2003; Ginoux, 2003]. Dry deposition follows the resistance-in-series approach and accounts for sedimentation, surface type, and meteorology following Wesely [1989]. Wet removal is based on Liu *et al.* [2001], which parameterizes large-scale in-cloud and below-cloud scavenging as a function of rainfall production rate and precipitation fluxes, respectively, and scavenging in convective updrafts as a function of the updraft mass flux. As has been done in previous studies [e.g., Colarco *et al.*, 2010], for both large-scale and convective-scale wet removal processes, we tune the scavenging efficiency to be 0.3 for dust (it is typically 1.0 for hygroscopic aerosols, as it is for the sea-salt aerosols in this study).

2.4. Dust Optical Properties

The focus of this study is the impact of the dust optical properties on the radiative fluxes and associated changes in the atmospheric circulation simulated in GEOS-5. We approach this by varying the assumptions of dust refractive index and particle shape in generating the lookup tables of dust optical properties used by the model. Recall that shape is considered for optical purposes only; we do not investigate the impact of shape on, for example, sedimentation velocities. We do not explicitly consider mineralogy or how it might vary with source regions, particle size, or during transport. Rather, we prescribe a size-independent refractive index that varies only with wavelength. The dust optical properties will affect the simulation as far as the radiative feedback on the model, and hence the dust lifecycle, but in all other respects the treatment of dust is as described in section 2.3 and is the same for each sensitivity study.

The dust refractive indices are drawn from three sources: (1) the Optical Properties for Aerosols and Clouds database [OPAC, Hess *et al.*, 1998], (2) the Shettle and Fenn [Shettle and Fenn, 1979, hereafter referred to as SF] database, and (3) a merger of remote sensing based estimates of dust refractive indices in the shortwave with the SF values in the longwave (referred to hereafter as OBS). The OBS-based refractive indices are from Colarco *et al.* [2002] in the UV (based on simulating the aerosol index from the Total Ozone Mapping Spectrometer) and from Kim *et al.* [2011] in the visible (based on inversions of the Aerosol Robotic Network Sun photometer observations). A log-power law curve is fit to the Colarco *et al.* [2002] and Kim *et al.* [2011] refractive indices, joining these smoothly with the SF refractive indices at infrared wavelengths. The real and imaginary components of the refractive index for each of these data sets are shown in Figure 1. We note that these data sets are used to varying degree by the modeling community. For example, the OPAC data set has been used for dust optical properties in studies by Perlwitz *et al.* [2001] and Colarco *et al.* [2010]. The SF data set drove the forcing calculation by Yi *et al.* [2011] discussed in the introduction. The OBS data set is arrived at partially from transport model simulations and is applied here to shortwave forcing calculations for the first time. For comparison, we also show the shortwave refractive indices used in Räisänen *et al.* [2012], which are from Haapanala *et al.* [2012, Table 1] and based on Sokolik and Toon [1999] and Kinne *et al.* [2003]. We note that the refractive indices tabulated in Haapanala *et al.* [2012] are less absorbing than the refractive indices considered in our simulations.

The optical properties of spherical dust particles are computed using the Mie theory code of Wiscombe [1980]. For each of our eight size bins we compute and then integrate the optical properties across 10 subsize bins assuming $dM/d(\log r) = \text{constant}$ across the size bin.

The optical properties of nonspherical dust particles are derived from the database of Meng *et al.* [2010], which is a compilation of optical properties for randomly oriented triaxial ellipsoids based on a combination of the solutions derived from Mie theory, the T-Matrix method [Mishchenko and Travis, 1998], the discrete dipole approximation (DDA) technique [Yurkin *et al.*, 2007], and an improved geometric optics method [Yang and Liou, 1996]. The electromagnetic edge effects [Nussenzweig, 1992] are included in the extinction and absorption cross sections for large size parameters in the geometric optics domain. The nodes in the database are refractive index, size parameter, and two values of particle aspect ratio.

Two particle shape distributions are considered for computing the optical properties of nonspherical dust: (i) a distribution composed primarily of triaxial ellipsoids based on Yi *et al.* [2011] and (ii) a spheroidal distribution from Dubovik *et al.* [2006]. Spheroids are a special case of triaxial ellipsoids and so are encompassed by the Meng *et al.* [2010] database (see their Figure 1). Compared to the integration for spherical properties discussed above, for both nonspherical shape distributions used here we are assuming volume equivalence. That is, for a given mass of dust in a particular size bin the total aerosol volume is the same regardless of whether spheres, spheroids, or ellipsoids are assumed for the shape distribution. This equivalence was shown

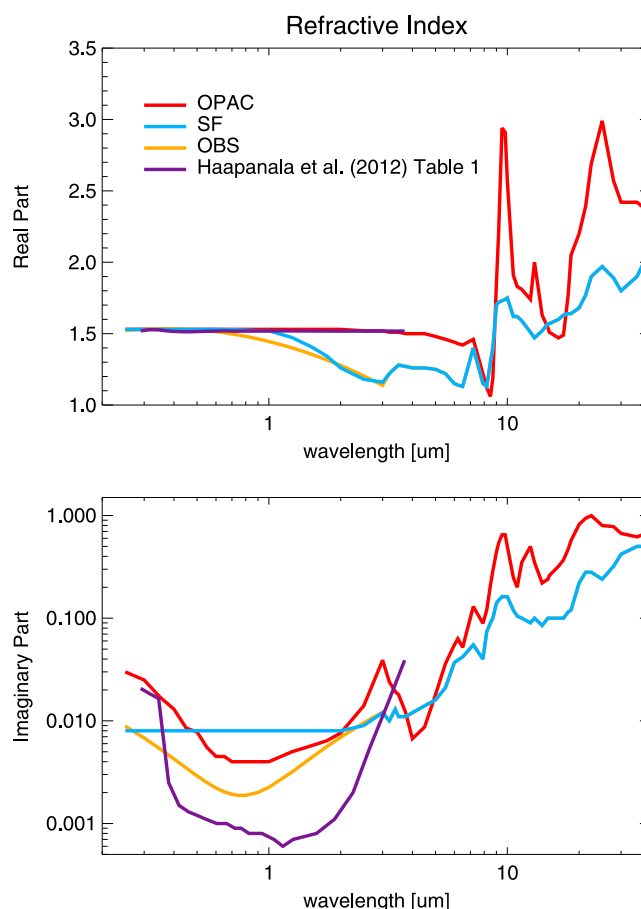


Figure 1. Spectral refractive indices used in this study for the OPAC, SF, and OBS simulations. Note that the OBS curve (the orange curve) is identical to the SF curve for wavelengths greater than 3 μm . Also shown are the shortwave refractive indices from Haapanala et al. [2012], used in Räsänen et al. [2012].

in Räsänen et al. [2012] to yield similar radiative fluxes and aerosol heating rates when nonspherical and spherical dust optics were compared for the same aerosol mass loading and size distribution versus other possible configurations (e.g., conserving projected surface area rather than volume). For each of our eight size bins, we integrate across a subsize bin distribution similar to what was done for the Mie theory calculations, with a second integration across the shape distribution. We note that the two shape distributions considered here are only two of many possible shape configurations suggested in the literature [e.g., Kalashnikova and Sokolik, 2004; Haapanala et al., 2012]. Furthermore, in order to consider the nonspherical shape effect on longwave radiative fluxes, we have used the same shape distributions for both our shortwave and longwave calculations. This is not strictly justified as the chosen shape distributions were arrived at through fitting shortwave observations. Our choice is thus pragmatic as we lack comprehensive observational information on the dust shape impact on longwave radiative fluxes.

Optical properties computed include the mass scattering and extinction efficiencies, asymmetry parameter, and the Legendre polynomial moments of the polarized phase function. Properties are computed at 61 wavelengths spanning 0.25–40 μm (the wavelengths considered in the OPAC database). The Meng et al. [2010] database encompasses the range of refractive index and size parameters considered in this study. Properties are integrated to the eight shortwave and ten longwave bands used in the GEOS-5 radiation codes using a simple linear averaging. Ultimately, we provide GEOS-5 a lookup table of the relevant optical properties (mass extinction efficiency, single scattering albedo, and asymmetry parameter) for each size bin and wavelength band.

Table 1 summarizes the configuration of optical properties used in each of our simulations. Figure 2 illustrates the spectrally varying dust optical properties— aerosol optical thickness (AOT), single scattering albedo (SSA),

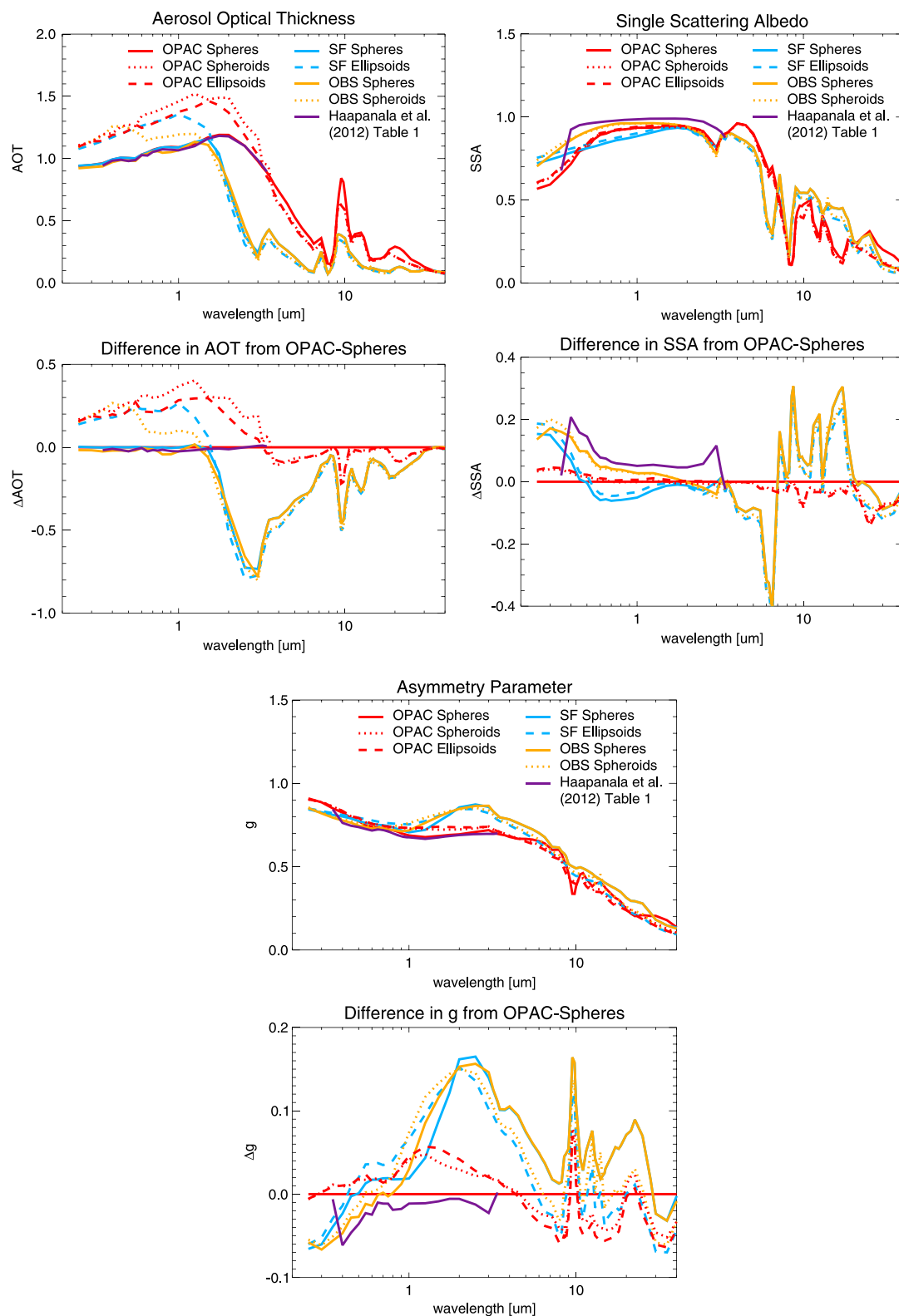


Figure 2. (Top, left) Spectral aerosol optical thickness (AOT), (top, right) single scattering albedo (SSA), and (bottom) asymmetry parameter (g) for each of our optical lookup tables considered in this study. Results presented are for the climatological particle size distribution at Cape Verde from our OPAC-Spheres simulation normalized to an AOT of 1 at 550 nm. For each panel, absolute values (top) and differences from the OPAC-Spheres values (bottom) are presented.

and asymmetry parameter (g)—for each of these experiments. For purposes of illustration, the GEOS-5 simulated summertime climatological and column-integrated particle size distribution for the OPAC-Spheres model run at Cape Verde (Figure 8, under the main Saharan dust plume) is used to compute the optical properties shown in Table 1 and Figure 2. The effective radius of this particle size distribution is $1.63\text{ }\mu\text{m}$, and the total aerosol loading has been normalized to give an AOT of 1 at 550 nm for the OPAC-Spheres set of optical properties. It is worth emphasizing here that these extrinsic aerosol properties are a strong function of the particle size distribution. If, for example, our model weighted the simulated dust mass toward larger particles we would have a lower SSA for the same choice of refractive indices. Also shown are the differences of AOT, SSA, and asymmetry parameter from the baseline of the OPAC-Spheres properties. Included in Figure 2 also are the shortwave spectrally varying properties computed assuming spheres and using the *Haapanala et al.* [2012] refractive indices shown in Figure 1. Figure 2 can be compared then with *Räsänen et al.* [2012, Figure 1], which shows a similar enhancement of AOT and asymmetry parameter for nonspherical particles versus spheres, and comparable spectrally varying properties for the *Haapanala et al.* [2012] refractive indices (although we used a different particle size distribution here). The dust optical properties shown in Figure 2 are summarized for a wavelength of 550 nm in Table 1. For comparison, for spheres and the *Haapanala et al.* [2012] refractive indices, the values are $\text{AOT}_{550} = 0.99$, $\text{SSA}_{550} = 0.96$, and $g_{550} = 0.73$. The range of single scattering albedo (0.82–0.93 at 550 nm) and asymmetry parameter (0.74–0.78 at 550 nm) shown in Table 1 and Figure 2 suggest possibly large differences in the simulated radiative forcing of dust as a function of the choice of optical properties. We explore this further in section 4.

2.5. Sea Salt

Sea-salt aerosol was also simulated simultaneously but externally mixed with the dust. Eight size bins were used here as well, ranging from 0.03 to $10\text{ }\mu\text{m}$ dry radius. The treatment of sea salt is similar to that described in *Colarco et al.* [2010]. The source formulation of *Gong* [2003] was used to determine emissions and the particle size distribution. Emissions occur only over open ocean and are a function of the 10 m wind speed. Sea salt aerosol is hydrated according to the parameterization of *Gerber* [1985] as a function of size and relative humidity. The hydration of the aerosol affects its fall velocity and optical properties. The sea-salt aerosols are radiatively coupled to GEOS-5, with optical lookup tables generated assuming Mie theory and similar for dust. Refractive indices for the dry salt particles are from the OPAC database. The hydrated optical properties are computed as a function of relative humidity, with water refractive indices from the HITRAN database [*Rothman et al.*, 2009] and assuming a volume average refractive index of the salt and water droplet. The sea-salt results are nearly identical in all of our dust sensitivity simulations, and so we do not discuss them further.

2.6. Experimental Design

We have run a series of simulations in which we changed the input dust optical properties (shape and refractive index) to our model. We have nine potential sensitivity experiments to consider: three sets of refractive indices and three shape distributions (spheres, spheroids, and ellipsoids) for each. We have completed seven of these simulations that include the radiative effects of dust and sea salt aerosols (see Table 1), as well as an additional simulation in which the aerosols were not radiatively active in the model (our “No Forcing” run). The differences in the absorption and scattering due to the choice of optical properties—illustrated in Figure 2—result in differences in radiative forcing of the atmosphere in our model across this set of simulations. This in turn feeds back on the dust aerosol lifecycle simulated. In section 3 we will illustrate significant differences in dust emissions, burden, and transport resulting from the different atmospheric forcings. In section 4 we will explore how differences in the dust distributions and optical properties impact the radiative fluxes calculated. For all of our simulations we maintain present-day concentrations of greenhouse gases and solar forcing. We use an annually repeating sea surface temperature database based on a climatology of sea surface temperatures from El Niño-neutral years [*Hurwitz et al.*, 2011]. The model is run at $2^\circ \times 2.5^\circ$ horizontal resolution with 72 vertical sigma layers from the surface to about 85 km altitude. A total of 16 aerosol tracers is carried (eight for dust and eight for sea salt). The dynamical and chemical time steps were 1800 s.

For each simulation the model is initialized with zero aerosol mass concentration beginning in model year 2003. The model is run for the period 2003–2050, discarding the results from 2003–2010 as simulation spinup. We mainly analyze the climatology of results for the 40-year period 2011–2050. Despite the imposed sea surface temperatures and the relatively short atmospheric lifetime of dust and sea salt aerosols, there is

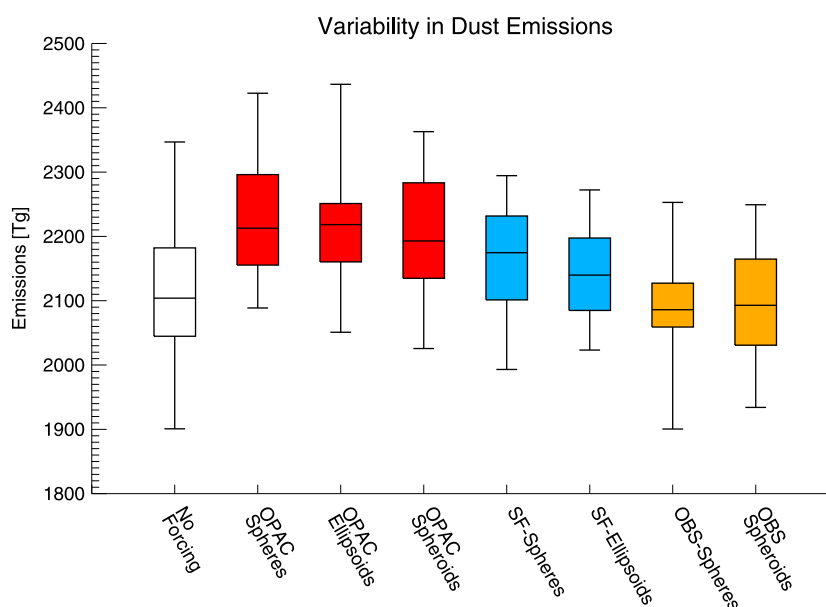


Figure 3. Years 2011–2050 climatology of annual mean dust emissions [Tg yr^{-1}] for each of our simulations. We show the mean (horizontal line), inner two quartile range (box), and extrema (whiskers) of the time series.

considerable interannual variability in the model results owing to the high sensitivity of dust emissions to the surface wind fields (equation (1), and see also the range of dust emissions in Figure 3), and so the relatively long integration time is performed to ensure statistically meaningful results.

3. Dust Simulation Evaluations and Comparison to Observations

In this section we evaluate the dust aerosol lifecycle simulated in GEOS-5. We focus first on various aspects of the mass budget to put our simulations in the context of other aerosol transport models. We also compare the dust mass and spatial distribution—including aerosol optical thickness, particle size distribution, and vertical profile—to available data sets in order to establish the overall credibility of our simulations. We consider the sensitivity of these model results to the choice of dust optical properties, but will more completely explore the aspects of the dust radiative forcing in section 4.

3.1. Dust Emissions

Figure 3 shows the climatological global annual mean dust emission magnitude of each of our simulations. The annual mean dust emission magnitude across our simulations is $2095\text{--}2221 \text{ Tg yr}^{-1}$. There is considerable interannual variability, and the overall range is between about $1900\text{--}2400 \text{ Tg yr}^{-1}$. North African dust emissions were in the range $1446\text{--}1556 \text{ Tg yr}^{-1}$. The difference between the high and low mean emissions is thus about 5%. Our emissions are similar in magnitude to the multiyear simulations presented in the GEOS-4 based version of our modeling system that employed the same particle size range and essentially the same dust mobilization scheme (1970 Tg yr^{-1}) [Colarco *et al.*, 2010]. Recent results from the Aerosol Comparisons between Observations and Models (AeroCom, <http://aerocom.met.no>) assessment of dust transport models shows global, annual dust emissions in the range of $1000\text{--}4000 \text{ Tg yr}^{-1}$ for models simulating particles in the same particle size range as in our simulations [Huneeus *et al.*, 2011].

Emissions in our simulations are generally the lowest for the No Forcing simulation. Highest emissions are for the simulations using the OPAC refractive indices, followed by the SF simulations, and finally the OBS simulations, which have similar emission magnitude to the No Forcing case. Shape has a minor impact on the simulation mean emissions compared to refractive index. The climatological annual mean and standard deviation of emissions for each simulation are presented in Table 2.

Figure 4 shows the climatological, seasonal average dust emissions from our No Forcing simulation for December–January–February (DJF), March–April–May (MAM), June–July–August (JJA), and September–October–November (SON) over the period 2011–2050. Strong dust sources are evident across northern Africa, including the sources

Table 2. Mean Aerosol Budget Diagnostics for Our Simulations, Including Emissions, Atmospheric Burden, Removal Rates, Lifetime, and AOT^a

Experiment Name	Emissions ^b (Tg yr ⁻¹)	North African Emissions (Tg yr ⁻¹)	Burden (Tg)	k_{wet} (day ⁻¹)	k_{dry} (d ⁻¹)	τ (day)	AOT
No Forcing	2107 ± 93	1446 ± 83	20.82 ± 0.75	0.081	0.194	3.63	0.019
OPAC-Spheres	2221 ± 86	1556 ± 78	23.10 ± 0.88	0.078	0.187	3.77	0.022
OPAC-Spheroids	2200 ± 83	1548 ± 69	23.08 ± 0.88	0.077	0.183	3.85	0.028
OPAC-Ellipsoids	2212 ± 80	1539 ± 79	23.08 ± 0.84	0.080	0.190	3.70	0.028
SF-Spheres	2161 ± 79	1504 ± 76	22.66 ± 0.82	0.078	0.185	3.80	0.021
SF-Ellipsoids	2138 ± 70	1481 ± 63	22.50 ± 0.70	0.076	0.180	3.92	0.028
OBS-Spheres	2095 ± 76	1448 ± 69	20.91 ± 0.65	0.080	0.190	3.70	0.019
OBS-Spheroids	2099 ± 87	1453 ± 78	20.93 ± 0.79	0.080	0.195	3.65	0.024

^aAll quantities are computed globally except for North African emissions.

^bThe ± indicates the standard deviation.

associated with the Bodele Depression and Lake Chad (most active in DJF), the eastern Libyan desert, northern Sudan, and across Mali, Mauritania, Algeria, and Western Sahara (see Prospero *et al.* [2002] for an environmental description of major dust source regions). Other major sources appear in northwestern India (most active in JJA), across Saudi Arabia and Iraq, and near Lake Eyre in Australia. Less intense dust emission regions include most of Australia, northern Mexico and the western United States, across Argentina and Chile, southern Africa, and more broadly across Asia and China. The Asian dust emissions appear particularly anemic in this model relative to other models [e.g., Ginoux *et al.*, 2004]. Preliminary studies with higher spatial resolution versions of the GEOS-5 modeling system (not shown here) suggest that spatial resolution is a key ingredient in determining realistic

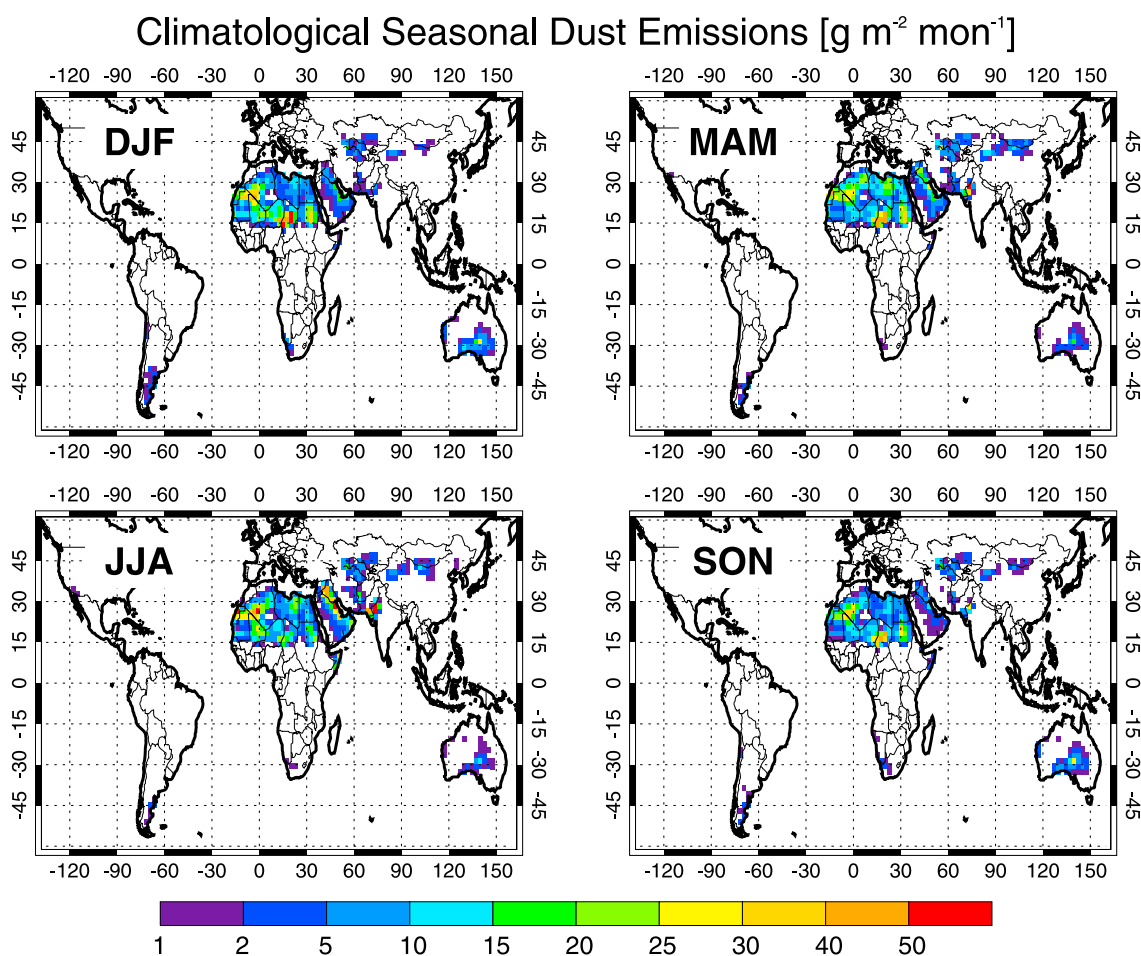


Figure 4. Years 2011–2050 climatology of seasonal dust emissions for our No Forcing simulation.

emissions from Asian dust sources because of the complex interplay of topography and surface winds in the Takla Makan and Gobi deserts in China. The coarse resolution of the topographic features in our simulations here does not develop the strong downslope wind features in these regions that drive real-world dust emissions. Some groups have attempted to correct for these deficiencies in coarse spatial resolution climate models by imposing distribution functions on the grid box mean wind speeds [e.g., *Cakmur et al.*, 2004; *Su and Toon*, 2009]. We do not implement such a scheme here. Despite this shortcoming over the Asian source regions, we find a higher degree of fidelity between the coarse and fine spatial resolution versions of our model for Saharan dust sources, which is in any case the globally dominant dust source (Table 2). Accordingly we focus our evaluation and analysis on Saharan dust.

3.2. Dust Mass Budget

In addition to summarizing emissions, Table 2 presents a summary of characteristics of the dust mass budget in each of our simulations. The global, annual mean dust aerosol burden in our simulations is in the range 20.8–23.1 Tg. The burden follows a similar pattern to the emissions, with the No Forcing and OBS simulations having the lowest burden, while the OPAC and SF simulations have the highest. There is only about a 5% range in the mean annual emissions between the simulations, whereas for the burden the range is closer to about 10% (20.82 Tg for No Forcing versus 23.10 for OPAC-Spheres). The simulated dust burden presented here is less than the burden of 31.6 Tg found in *Colarco et al.* [2010], and the aerosol residence time is correspondingly found to be shorter in the present study (3.63–3.92 days) than in *Colarco et al.* [2010]. There are important differences between the GEOS-5 based model and the GEOS-4 system used in *Colarco et al.* [2010]: the physical parameterizations for turbulence, convection, and precipitation are entirely different, which have significant impacts on the aerosol transport and removal, and the GEOS-4 simulations were run with assimilated meteorology, whereas here we are running climate simulations. The shorter dust aerosol atmospheric residence time and lower dust burden here are more consistent with the mean of models participating in the Aerosol Comparisons between Models and Observations (AeroCom) project (19.2 Tg and 4.22 days, respectively, see *Textor et al.* [2006]; see also the updated values of 15.8 Tg and 4.6 days, respectively, in *Huneus et al.* [2011]). We note the generally greater residence time in the OPAC and SF simulations compared to the No Forcing and OBS simulations (e.g., 3.63 days for No Forcing versus 3.92 days for the SF-Ellipsoids simulation).

Also shown are the dust wet and dry loss frequencies defined as in *Colarco et al.* [2010], which provide an indication of relative importance for loss processes. The wet loss rate in our simulations is in the range 0.076–0.081 day^{−1}, compared to 0.055 day^{−1} in our GEOS-4 simulations [*Colarco et al.*, 2010] and 0.084 day^{−1} for the median of the AeroCom models reported in *Textor et al.* [2006]. The dry loss rate is in the range 0.180–0.195 day^{−1} here, compared to 0.116 day^{−1} for our GEOS-4 simulations and 0.245 day^{−1} for the AeroCom mean. The discussion of the loss rates and lifetimes presented here is to put our model in the context of other aerosol models, but there is clearly diversity among those various models. Intermodel differences arise from different parameterizations of loss processes, as well as model physics, spatial resolution, and meteorology. Even with respect to comparison with our GEOS-4 simulations it is important to note that the GEOS-4 results came from an older version of our modeling system that was driven by meteorological reanalyses and incorporated different model physics, whereas here the simulations are from a free-running climate model.

Figure 5 and Table 3 present a comparison of our climatological annual simulated dust surface mass concentration to the multiyear annual mean of measurements at 22 sites. The data presented are the same as shown in *Huneus et al.* [2011], deriving from the long-term measurements managed by the Rosenstiel School of Marine and Atmospheric Sciences at the University of Miami (AEROCE) [*Prospero et al.*, 1989; *Prospero*, 1996; *Arimoto et al.*, 1995]. These sites are located mainly far downwind of dust source regions, and the concentration of dust is obtained from high volume air samplers by measuring aluminum concentrations after collected filters are ashed in an oven (assuming aluminum content is 8% of total dust mass). Figure 5 shows the comparison for our OPAC-Spheres model run, also summarized in Table 3 (results for all simulations are in Table S1 in the supporting information). Our model is well correlated in the multi-year annual mean with the observations, although it generally underestimates the mass in the central Pacific sites. Performance appears to be best for sites impacted by Saharan dust, with discrepancies between the model and observations mostly within a factor 2–3. For the comparisons to data presented here and elsewhere in this study it is important to point out that we are comparing the model climatological fields (whether

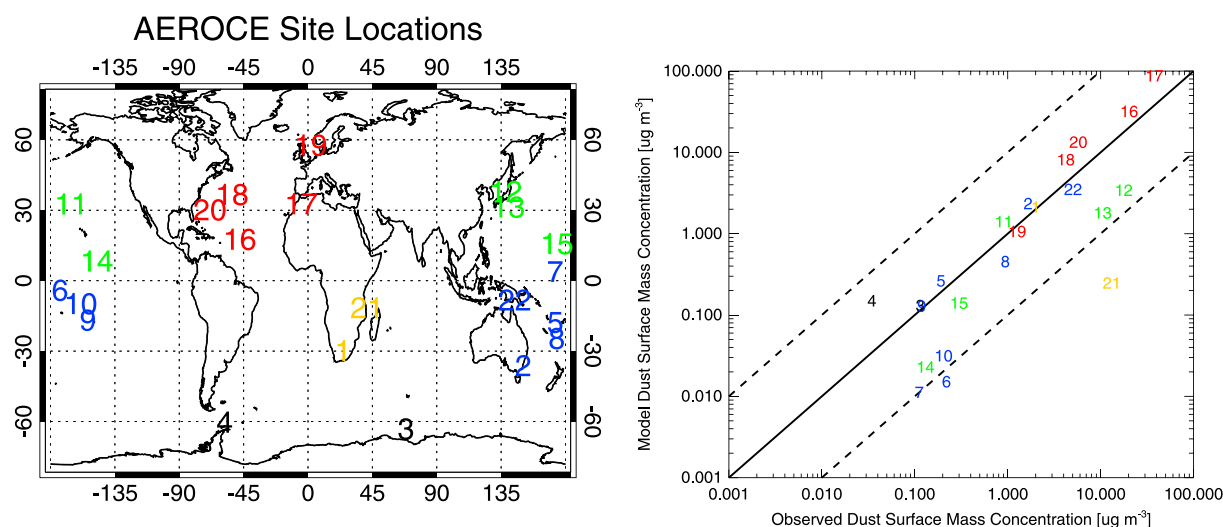


Figure 5. Map of dust surface mass concentration sites summarized in Table 3. Also shown is a scatterplot of the OPAC-Spheres modeled climatological mean surface mass concentration compared to the multiyear observations at each site. The one-to-one line is indicated by a solid line. The dashed lines show the 10-to-1 and 1-to-10 lines. Colors correspond to broad geographical regions to facilitate analysis of scatterplot.

monthly, seasonal, or annual) to long-term averages of the various data sets used, and that we are not simulating particular events captured in those data sets.

Comparisons of our OPAC-Spheres model run to multiyear observations of dust deposition are shown in Figure 6, with site locations and details for all of our model runs presented in Tables S2 and S3. Again, the data are as presented and screened in *Huneeus et al.* [2011] and are derived from measurements taken during the Sea/Air Exchange field campaign (SEAREX, *Prospero et al.* [1989], with data as presented in *Ginoux et al.* [2001]), measurements presented in *Mahowald et al.* [2009], and the Dust Indicators and Records in Terrestrial and Marine Paleoenvironments data set (DIRTMAP) [*Tegen et al.*, 2002; *Kohfeld and Harrison*, 2001]. The model is generally underestimating dust deposition, particularly in the remote Pacific locations, and is overestimating in the remote regions near Antarctica but is otherwise generally within a factor of 10 of the observations and within a factor of about three to five at sites near western African, immediately downwind of Saharan dust sources.

Table 3. Comparison of Climatological Mean Dust Surface Mass Concentration From the OPAC-Spheres Model Run to Multiyear Mean of Measurements From *Prospero et al.* [1989], *Prospero* [1996], and *Arimoto et al.* [1995]

Site #	Site Name	Years	Lat	Lon	Elv [m]	Observed [$\mu\text{g m}^{-3}$]	Model [$\mu\text{g m}^{-3}$]
1	Cape Point, South Africa	1992–1996	34°20'S	18°28'E	249	1.78	1.82
2	Cape Grim, Tasmania	1983–1996	40°40'S	144°40'E	94	1.48	2.00
3	Mawson, Antarctica	1987–1996	67°35'S	62°30'E	20	0.10	0.11
4	Palmer Station, Antarctica	1990–1996	64°46'S	64°02'W	10	0.03	0.13
5	Yate, New Caledonia	1983–1985	22°08'S	167°00'E	0	0.17	0.22
6	Funafuti, Tuvalu	1983–1987	08°30'S	179°11'W	0	0.20	0.01
7	Nauru	1983–1987	00°31'S	166°56'E	7	0.10	0.01
8	Norfolk Island	1983–1997	29°04'S	167°58'E	0	0.84	0.39
9	Rarotonga, Cook Islands	1983–1994	21°30'S	159°45'W	0	0.10	0.11
10	American Samoa	1983–1996	14°15'S	170°34'W	42	0.16	0.03
11	Midway Island	1981–1997	28°13'N	177°20'W	0	0.72	1.20
12	Cheju, South Korea	1991–1995	33°31'N	126°28'E	70	14.14	2.91
13	Hedo, Japan	1991, 1994	26°55'N	128°15'E	0	8.37	1.54
14	Fanning Island	1981–1986	03°53'N	159°19'W	4	0.10	0.02
15	Enewetak Atoll	1981–1987	11°19'N	162°19'E	0	0.24	0.12
16	Ragged Point, Barbados	1984–1998	13°10'N	59°25'W	41	16.15	27.18
17	Izana, Tenerife	1987–1998	28°18'N	16°30'W	2367	30.18	74.45
18	Bermuda (East & West)	1989–1998	32°16'N	64°52'W	51	3.36	6.93
19	Mace Head, Ireland	1988–1994	53°19'N	09°50'W	5	1.01	0.91
20	RSMAS–University of Miami	1989–1998	25°45'N	80°15'W	5	4.59	11.38
21	Rukomechi, Zimbabwe	Not Known	16°00'S	29°30'E	Unknown	10.53	0.21
22	Jabirun, N. Australia	Not Known	12°41'S	139°53'E	Unknown	4.03	2.98

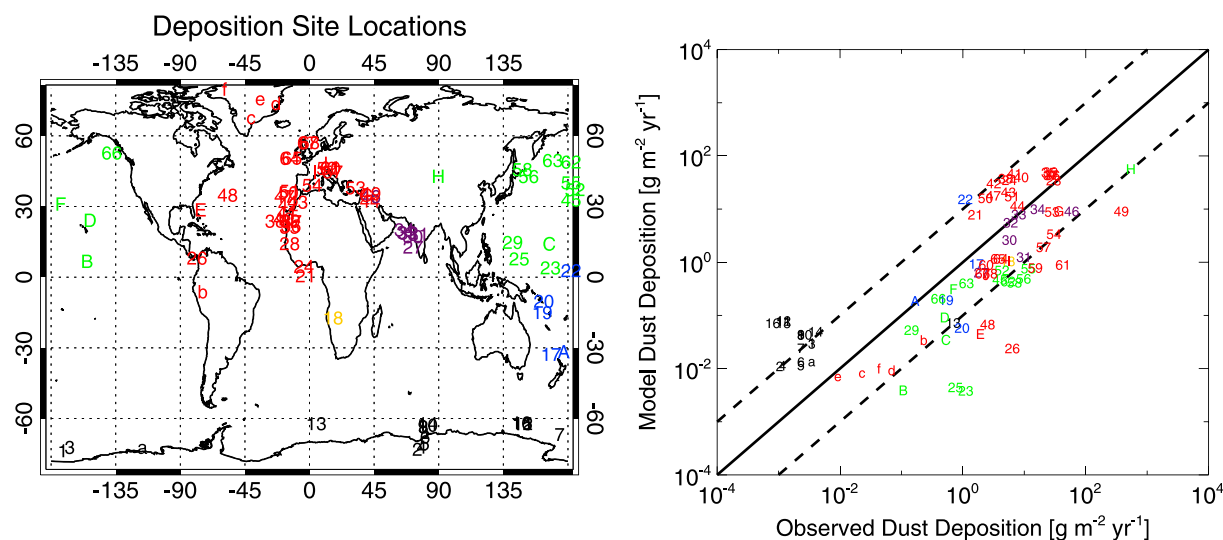


Figure 6. As in Figure 5 but dust deposition sites listed in Table S2.

3.3. Dust AOT

In Figure 7 we show the climatological, seasonal average dust AOT (at 550 nm) from our No Forcing simulation. Consistent with Figure 4, we see high dust AOT associated with the Bodele Depression in northern Africa peaking in DJF, the strong dust sources in western India peaking in JJA, and the peak of the Asian dust emissions

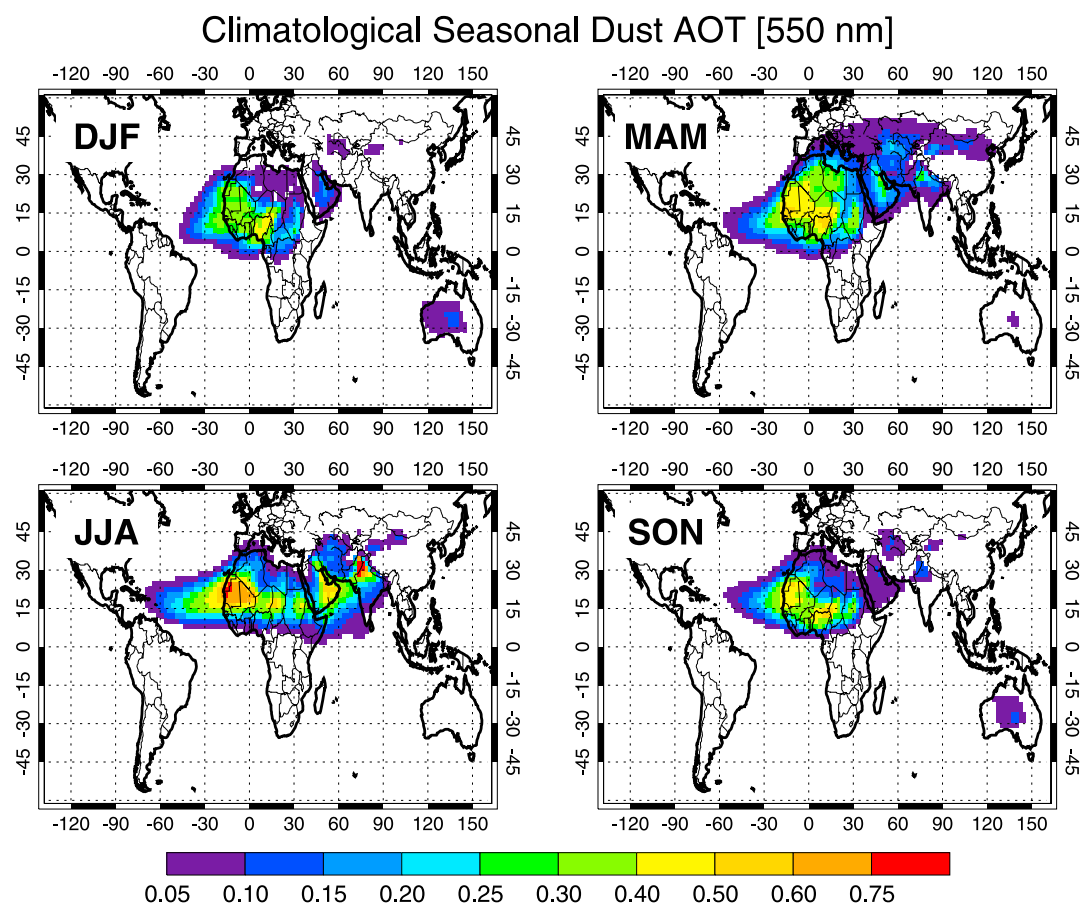


Figure 7. Years 2011–2050 climatology of seasonal 550 nm dust AOT for our No Forcing simulation.

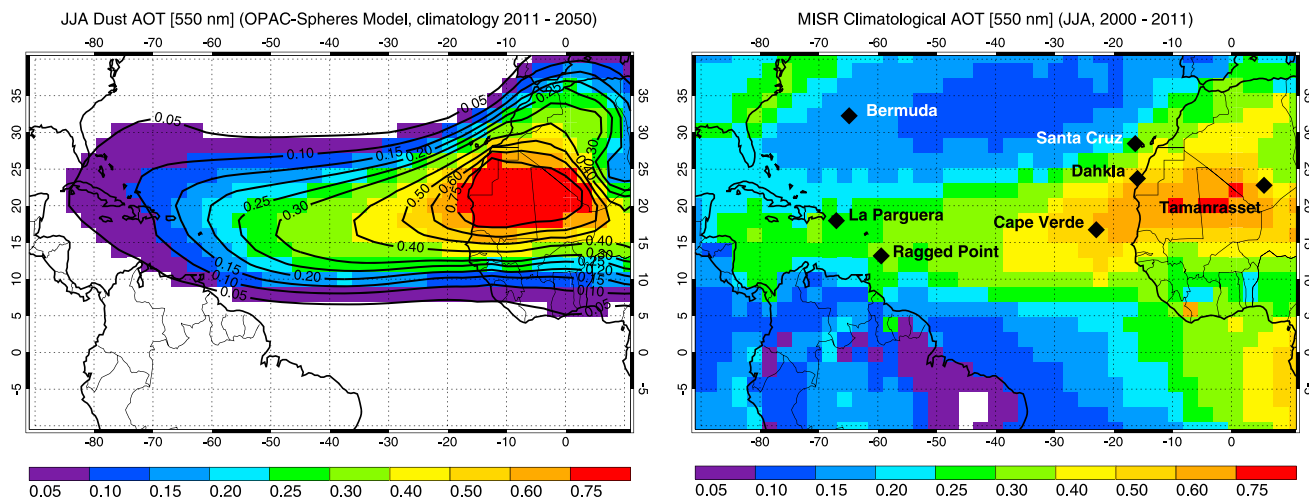


Figure 8. Climatological JJA dust aerosol optical thickness from the (left) OPAC-Spheres (shading) and No Forcing (contours) model runs (dust only) and (right) MISR observations. Also shown are the locations of the AERONET sites used in this study.

during MAM. The most evident feature remote from the source regions is the Saharan dust plume over the North Atlantic Ocean. This plume moves north and south with the seasonal progression of the inter-tropical convergence zone (ITCZ), with the peak of both its northward and westward transport occurring during JJA.

Figure 8 shows a comparison of our model 550 nm dust AOT over the northern Atlantic Ocean to observations retrieved by the Multi-angle Imaging Spectroradiometer (MISR) flying onboard the NASA Terra spacecraft. MISR measures reflected radiation in four visible channels from nine different cameras viewing the same scene at different angles as the spacecraft flies over. These 36 pieces of information permit cloud clearing and selection of an appropriate lookup table of aerosol radiative properties to retrieve AOT, among other aerosol characterization capabilities [Kahn *et al.*, 2005]. Since our model is not simulating the actual period of MISR observations we compare here our JJA model climatological dust AOT to the JJA climatology of MISR AOT for the period 2000–2011. We show in Figure 8 the simulated dust AOT from both our No Forcing and our OPAC-Spheres model runs. Both simulations used the same dust optical properties, the difference being whether aerosol forcing was turned on or not. Comparing these we clearly see the higher AOT in the OPAC-Spheres run consistent with higher dust emissions, as well as a farther westward transport of the dust plume over the Caribbean. In comparison to MISR, the OPAC-Spheres model run has a similar north–south placement of the dust plume, although the model AOT appears somewhat higher than the observations over the source regions. The MISR observations are additionally sensitive to other aerosols besides dust, as is evident in the pollution plume along the U.S. east coast and the features associated with biomass burning in South America and southern Africa.

Figure 9 shows the climatological JJA simulated 550 nm dust AOT for each of our simulations at four different longitudes west of northern Africa. Also shown is the 2002–2011 JJA climatology of the 550 nm AOT from the Moderate Resolution Imaging Spectroradiometer (MODIS) onboard the NASA Aqua spacecraft. MODIS retrieves over ocean AOT in cloud-free conditions from measurements of reflected radiation at six visible channels [Tanré *et al.*, 1997]. Similar to the MISR observations shown, we are not attempting to separate the dust AOT from the total AOT in the MODIS observations, but rather focusing on what the observations tell us qualitatively about our simulations. Near the source region (the slice at 20°W) the different simulations all have a peak in the dust AOT at about 20°N, consistent with the placement of the peak in the MODIS AOT. AOT is highest for the OPAC based simulations using nonspherical optics, consistent with the higher emissions in these simulations (Figure 3) and the enhanced mass extinction efficiency of the nonspherical optics (Figure 2). The north–south placement of the dust plume is similar for all of the model simulations, and consistent with the peak in the MODIS AOT out to 60°W. By 80°W this similarity with the MODIS observations has broken down. As the plume moves to the west, the No Forcing and OBS-based simulations (i.e., the least absorbing simulations) peak in AOT more toward the southern edge of the dust plume, while the OPAC and SF based simulations maintain a more uniform north–south distribution and higher AOT magnitude.

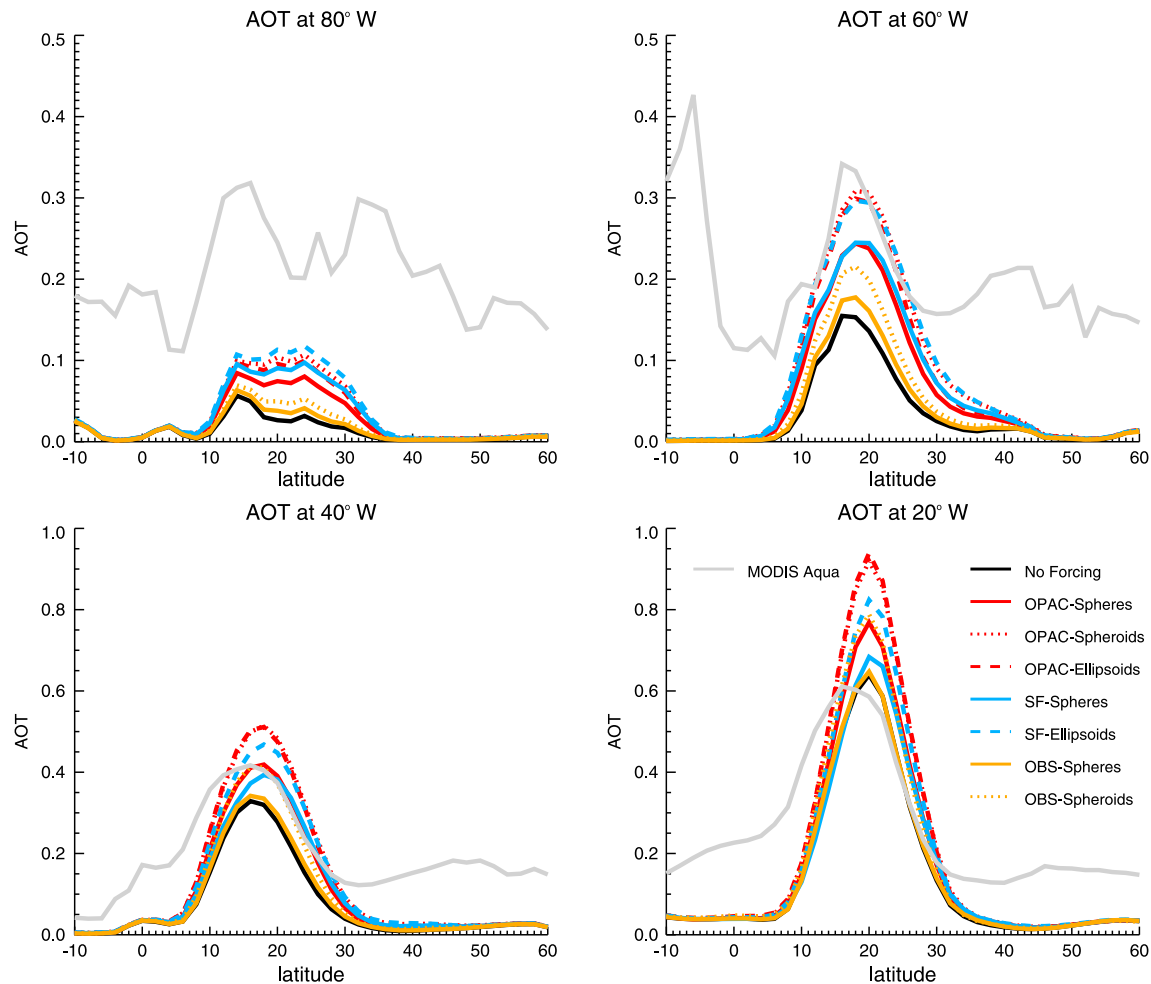


Figure 9. Climatological simulated JJA dust AOT at four different longitudes west of northern Africa. Also shown is the MODIS Aqua over ocean AOT climatology for JJA 2002–2011.

Figure 10 shows the climatological JJA simulated 550 nm dust AOT for each of our simulations across the North Atlantic Ocean averaged in the latitude band 10–30°N. For comparison we also show the JJA MODIS Aqua over ocean total AOT averaged over the period 2002–2011. In Figure 10(left) the results are plotted exactly according to the model output, and the difference in the model simulations due to optical assumptions and differences in

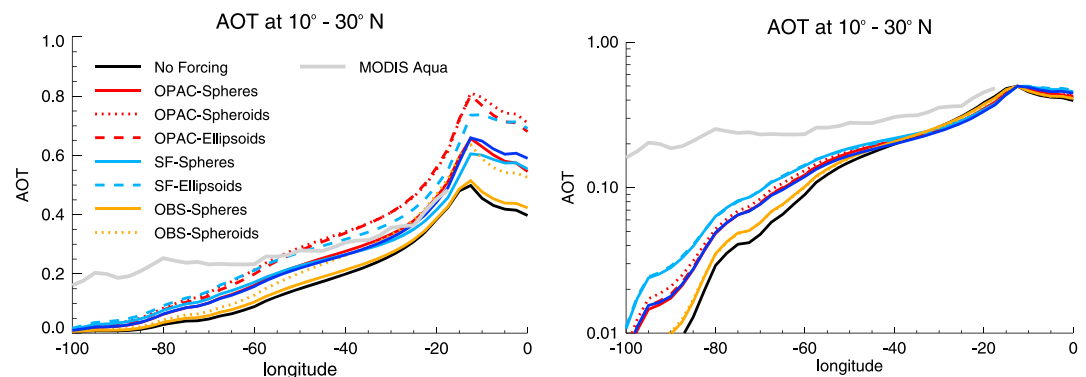


Figure 10. Climatological JJA dust AOT in the latitude band 10–30°N for our simulations for the years 2011–2050. Also shown is the climatological JJA MODIS Aqua over ocean AOT averaged over the period 2002–2011. (left) The results are plotted on a linear scale. (right) The model and satellite values are normalized to the same value of AOT at the longitude of Cape Verde and the results are plotted on a log-y axis to emphasize differences in the simulations.

emissions is clearly evident at the eastern longitudes, closest to the source regions. In Figure 10(right) the model and MODIS AOT are normalized to the same value of AOT at the longitude of Cape Verde (off the west coast of northern Africa, near the source region, see Figure 8) and the results are plotted on a log-y axis. This emphasizes the differences in the long-range transport of the dust from northern Africa, across the Atlantic, and into the Caribbean, showing that in a relative sense dust is transported farther west in the OPAC and SF-based simulations, while the OBS and No Forcing simulations are more similar with the least westward export of the dust plume. We will investigate the cause of this difference in section 4. Also evident is that the relative westward transport of the dust plume is largely insensitive to the shape assumptions, with the model results most clearly clustered according to refractive index in Figure 10(right). The MODIS observations lend some context, showing the diminishment of AOT as the plume propagates west of Africa, although clearly the model results fall off more rapidly than the satellite observations suggest. This could be due to too aggressive removal of aerosol in the model. In previous studies with our model we investigated the east-west gradient of dust AOT across the Atlantic and determined wet removal was too aggressive [Nowottnick *et al.*, 2011]. While we adopted Nowottnick *et al.*'s [2011] suggested changes to the scavenging parameters in the simulations presented here it seems this issue is persistent. We note that we are running an updated version of the model versus Nowottnick *et al.* [2011], and our simulations are at a coarser spatial resolution and in a climate mode versus being driven by assimilated meteorology. Alternatively, the MODIS observations of course also include aerosols other than dust, including sulfate and carbonaceous aerosols, which become an important component of the total AOT particularly in the westernmost longitudes and could bias our comparisons (see Figure 8(right)).

Figure 11 shows a comparison of the climatological monthly mean 550 nm dust AOT from each of our simulations compared to climatological monthly averaged observations from the Aerosol Robotic Network (AERONET) of sun/sky scanning photometers [Holben *et al.*, 1998]. AERONET observes attenuation of the direct solar beam in measuring AOT at a number of wavelengths, here interpolated to 550 nm wavelength. The AERONET site locations chosen are shown in Figure 8 and described in Table 4, which also shows the years and total number of monthly mean AOT values being used in Figure 11. Near the source region (Santa Cruz, Dahkla, Cape Verde, and Tamanrasset) the model has a similar seasonal cycle to the observed AOT, although the model tends to have a higher magnitude AOT relative to the observations, especially at Dahkla and Santa Cruz. At Tamanrasset, the simulated AOT is more comparable to the magnitude in the observations, although the seasonal cycle in the model is distinctly bimodal in all simulations while it is relatively flat between March and September in the observations. On the other hand, the seasonal cycle and magnitude are best simulated at Cape Verde, which is directly below the main summertime transport pathway.

Figure 11 also shows several sites impacted on the western edge of the dust plume (Bermuda, La Parguera, and Ragged Point). Bermuda is only marginally impacted by dust, as evidenced by the relatively high Angstrom parameters at that site (not shown). There is a clear difference here again between the No Forcing and OBS based simulations on the one hand and the OPAC and SF simulations on the other, showing the more pronounced northward transport in the OPAC and SF simulations while the No Forcing and OBS based simulations have a pronounced minimum in AOT during the summer months. At La Parguera the summertime Angstrom parameter is generally low, indicative of dust, and the seasonal peak in dust AOT magnitude in June and July is well represented in the model, although the model appears to shift the peak toward the earlier part of the season. Again, the distinction between the more absorbing SF and OPAC simulations versus the No Forcing and OBS simulations is clear, with much lower AOT in the latter set. This remains the case at Ragged Point, the furthest south site considered, where again the seasonal cycle and peak AOT magnitude are well represented by the model. At all three sites we compare the ratio of the June climatological simulated dust AOT between the SF-Spheroids and No Forcing simulations. The ratio is highest Bermuda (1.78), intermediate at La Parguera (1.59), lowest at Ragged Point (1.34). This indicates a relative preference for southward transport of the dust plume in the No Forcing model, which is also the case for the OBS based models. Incidentally, this ratio is lower than the Ragged Point value at all the near-source sites except Tamanrasset (where it is 1.44).

In summary, despite similarities in the dust emissions, burden, and lifetime, there is a wide range in the value of the global, annual mean dust AOT in our simulations (range is 0.019–0.028). The highest dust AOT values are associated with the model runs that incorporated nonspherical dust optics, owing to the higher visible wavelength mass extinction efficiency (i.e., AOT per unit mass) in the nonspherical cases (see Figure 2). The various simulations show similar AOT spatial and temporal variability as satellite and ground-based observations (see Figures 8–11), although there is a tendency of the model AOT to be somewhat higher in magnitude than the

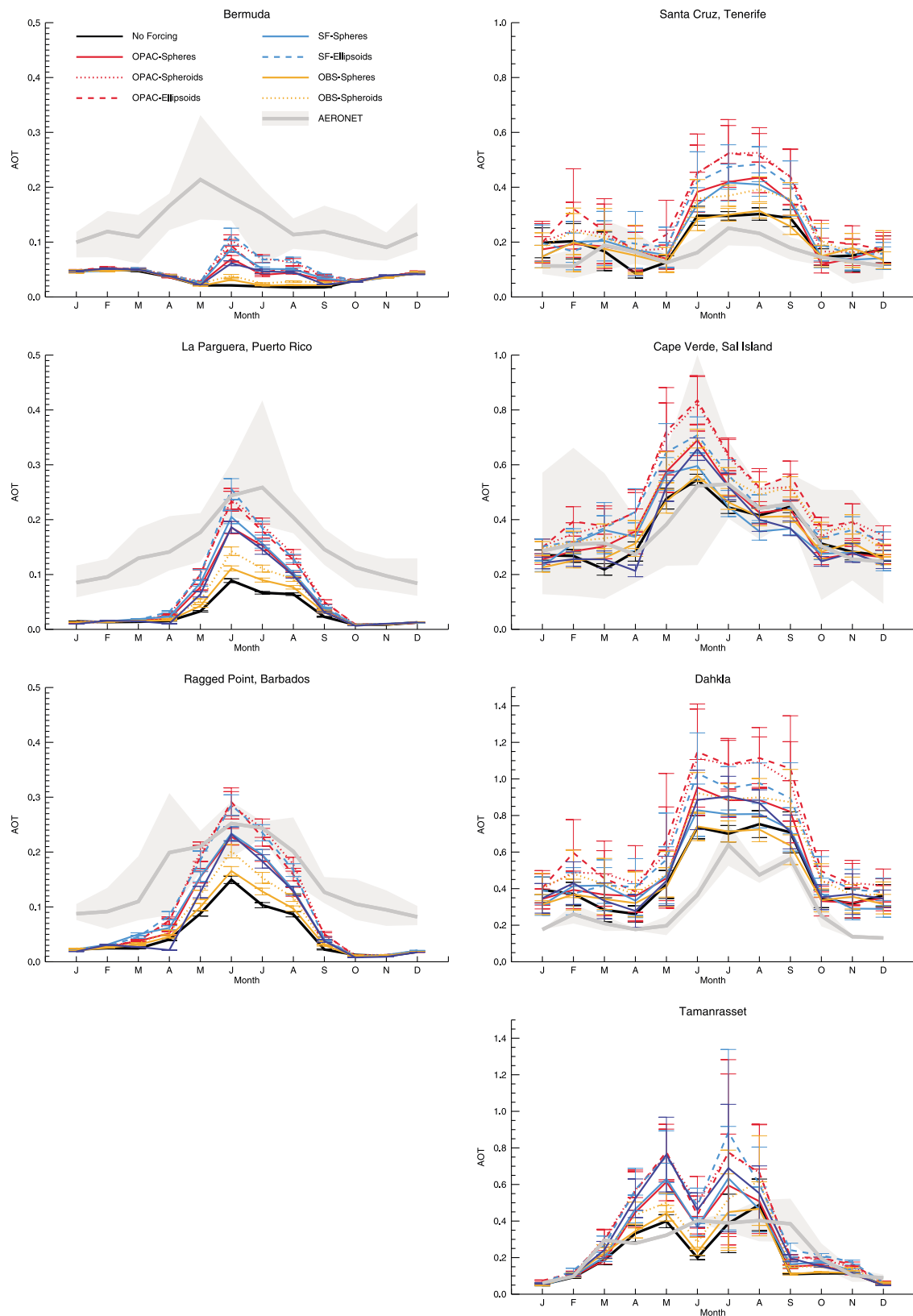


Figure 11. Comparison of climatological monthly mean AOT from our simulations to multiyear monthly means from AERONET at seven sites impacted by Saharan dust. The whisker bars indicate the standard deviation of the monthly mean values. The sites are described in Table 4 and their locations shown in Figure 8. The AERONET mean and standard deviations are indicated by the grey line and light grey shading.

Table 4. AERONET Sites Used in This Study^a

Site	PI	Years	Lat	Lon	Elv (m)	n_{aot}	n_{inv}
Ragged Point	Joe Prospero	2007–2011	13°09'N	59°25'W	40	52	11
La Parguera	Brent Holben	2000–2011	17°58'N	67°02'W	12	110	24
Bermuda	Brent Holben	1996–2002	32°22'N	64°41'W	10	64	10
Cape Verde	Didier Tanré	1994–2011	16°43'N	22°56'W	60	179	39
Santa Cruz	Emilio Cueva-Agullo	2005–2011	28°28'N	16°14'W	52	72	17
Dahkla	Hammad Bencheikroun	2002–2003	23°43'N	15°56'W	12	22	6
Tamanrasset	Emilio Cueva-Agullo	2006–2009	22°47'N	5°31'E	1377	24	6

^aIncluded are the responsible principle investigator (PI) at each site, the years active, the latitude (Lat), longitude (Lon), and elevation (Elv). Also indicated are the number of monthly mean AOT values used in constructing Figure 11 (n_{aot}) and the number of JJA monthly mean inversions used in constructing the seasonal particle size distributions shown in Figure 12 (n_{inv}).

observations, particularly near the Saharan dust sources. Nevertheless, the more moderate east-west gradient in AOT and the more northward shift of the dust plume in the OPAC and SF simulations suggest they agree better with the AERONET observations (Figure 11) than do the OBS and No Forcing simulations.

3.4. Dust Particle Size Distribution

Figure 12 shows a comparison of the volume dust particle size distribution simulated in the model to the retrieved particle size distribution from the AERONET measurements. Under high AOT (> 0.4) and

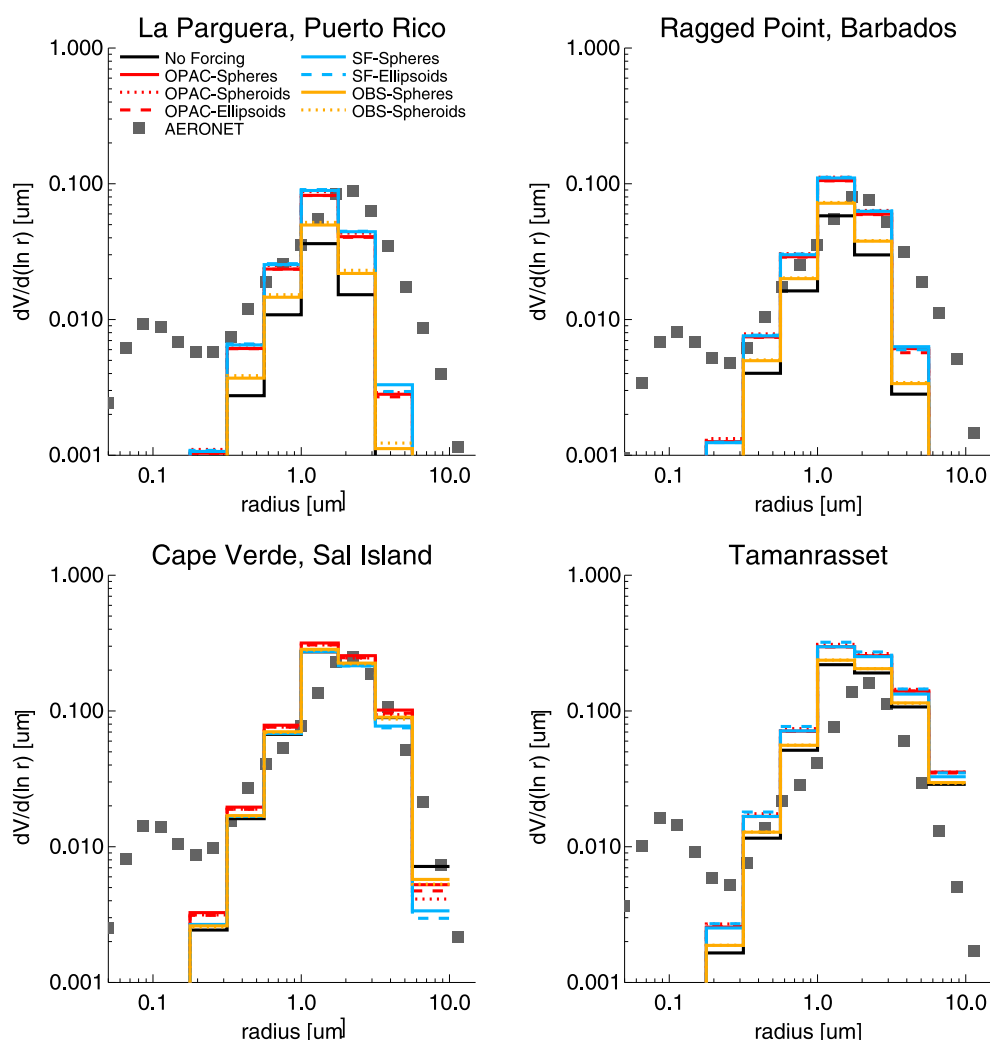


Figure 12. Comparison of JJA climatological simulated dust particle size distribution (lines) to the seasonal multiyear AERONET retrieved particle size distribution at four AERONET sites.

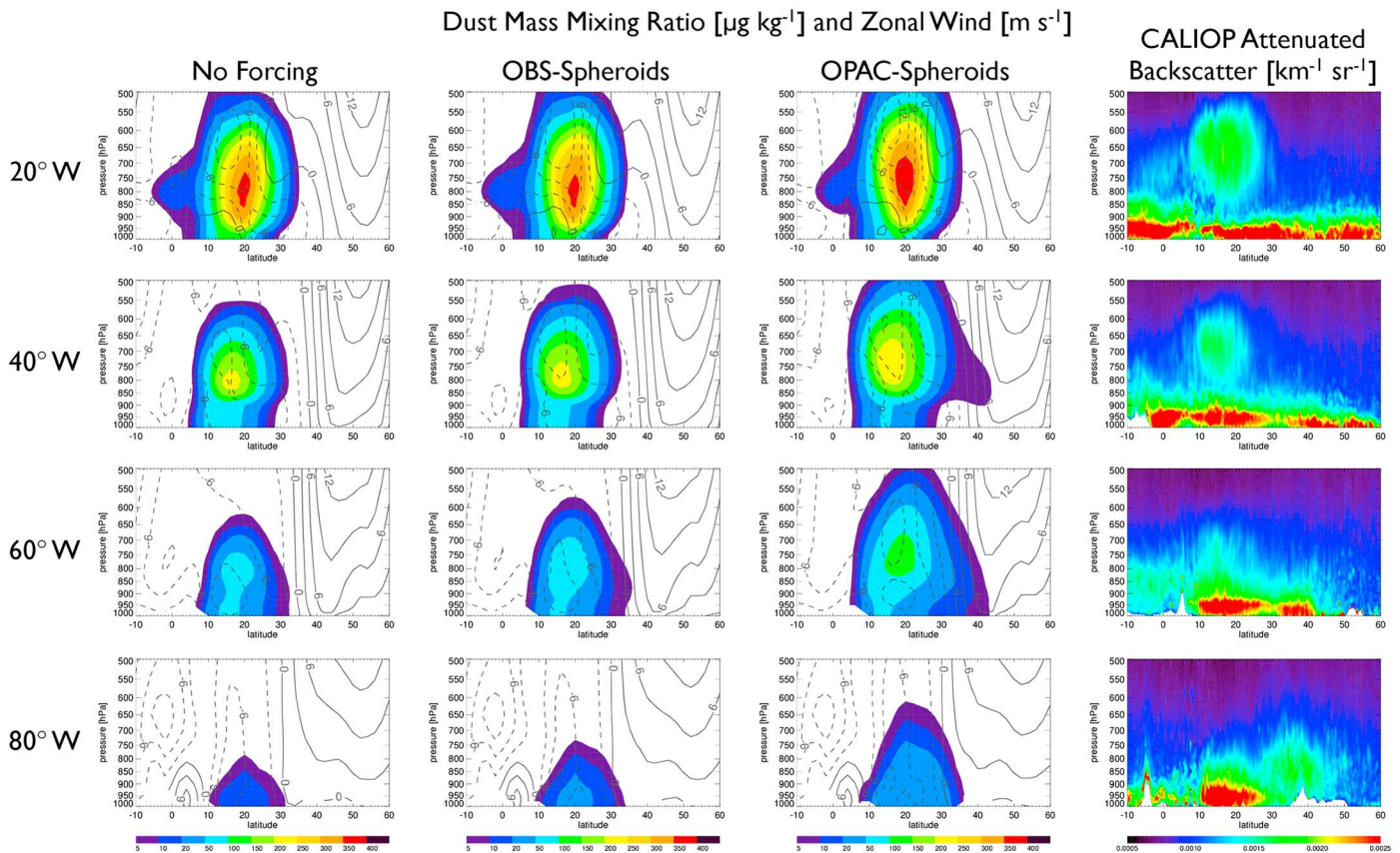


Figure 13. Simulated JJA climatological dust mass mixing ratio profiles at four longitudes west of the Saharan source region. Results are shown for three model simulations, as well as the year 2011 seasonal attenuated backscatter measured by CALIOP (right column). On the model plots we also show the profile of the climatological seasonal mean zonal wind. White regions at the surface in the CALIOP plots are below the local topography.

homogeneous sky conditions AERONET can invert column integrated particle size distribution from its almucantar scan [Dubovik and King, 2000]. For each of the sites shown we aggregated monthly mean particle size distributions from the AERONET data set during JJA (the number of individual months used at each site is indicated in Table 4). For comparison we show the climatological JJA column integrated particle size distribution from the model. Note that the AERONET retrievals all contain a fine mode component to the total particle size distribution (radius $< 0.5 \mu\text{m}$) that is absent in the model. This fine mode presumably corresponds to aerosols not simulated in the model. Near the source regions (Cape Verde and Tamanrasset), there is very little difference in the particle size distribution among the model runs. The model tends to peak in volume in the size bin spanning radius range $1\text{--}1.8 \mu\text{m}$, while the AERONET retrievals put the volume peak between about $2\text{--}3 \mu\text{m}$ radius. Farther from the source regions (La Parguera and Ragged Point), the peak in the simulated particle size distribution volume occurs in the same size bin as near the sources. However, larger particles, preferentially removed by sedimentation in the model, are relatively depleted compared to the retrievals at these distant sites. There are as well larger differences between the model simulations at these sites, owing to greater difference in the total loading at these sites.

3.5. Dust Vertical Profiles

Figure 13 shows a composite of the climatological JJA dust vertical profile from three of our model simulations at four longitudes west of northern Africa. The dust vertical profile is presented as the profile of the total dust mass mixing ratio. Also shown is the JJA 2011 aerosol attenuated backscatter profile measured by the Cloud-Aerosol Lidar with Orthogonal Polarization (CALIOP) flying aboard the NASA CALIPSO spacecraft. CALIPSO flies in a polar orbit in formation with the NASA Aqua spacecraft as part of the so-called “A-Train” of satellites. CALIOP profiles the atmosphere with a two-channel lidar system, measuring attenuated backscatter at 532 and 1064 nm and depolarization at 532 nm [Winker et al., 2010]. The comparison of the model

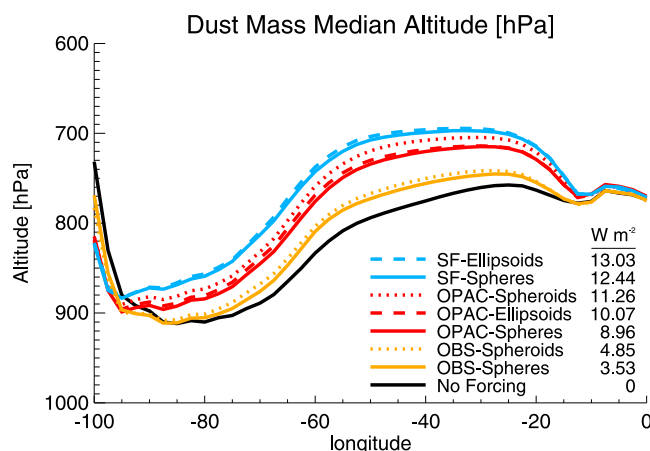


Figure 14. Dust median altitude for each of simulations. Results are shown for the JJA climatological mean value averaged in the latitude range 10–30°N. Labeling is sorted from (top) highest dust median altitude to (bottom) lowest, with the climatological, regional, over ocean, net all-sky dust atmospheric forcing in $W m^{-2}$ beside each label.

vertical profile to the CALIOP observations should be understood to be qualitative, as only a single season of the CALIOP observations are presented, and of course the CALIOP backscatter observations are sensitive to the presence of clouds and other aerosols besides dust. Still, the dust features seen in the CALIOP observations are fairly typical of the observed profiles, showing an elevated aerosol layer near the African coast (20° W) between about 850–550 hPa altitude and between about 10–25°N latitude. This is similar to the vertical placement of the aerosol plume in the model simulations shown, which peaks at about 20°N latitude and between about 850–700 hPa altitude. As the aerosol moves west the elevated dust plume is still evident in the CALIOP observations at 40°W at nearly the same latitudes, although in the model the plume has moved south to a centroid of around 15°N latitude. Further west the aerosol layer is less distinct in the CALIOP observations and essentially merges with boundary layer aerosols. The simulated profile descends farther toward the west, and it becomes evident that the dust retains its elevation more clearly in the OPAC-Spheroids simulation while in the OBS-Spheroids and No Forcing simulations it is at a lower altitude.

Figure 14 shows the northern Atlantic JJA climatological dust median altitude (the altitude at which half the dust column mass is above and below) for each of our simulations. This approach normalizes differences in the absolute column loading between the simulations. Over the dust source region, where aerosol mass is well mixed by the deep boundary layer, there is little difference between the simulations. When the dust is advected over the ocean, however, the differences in the simulations are immediately apparent, with the OPAC and SF simulations maintaining a much higher dust median altitude than either the OBS or No Forcing simulations. The difference in the median altitude is about 100 hPa between the SF and No Forcing simulations at about 60°W. These results are consistent with what is shown in Figure 13 and suggest an explanation for the higher AOT maintained by the SF and OPAC simulations across the Atlantic as shown in Figure 10: the relatively higher in altitude the dust mass remains during transport, the longer its atmospheric residence time and hence the farther west it may be transported. We discuss a mechanism for these differences in altitude in section 4.3.

4. Impact of Dust Distributions and Optical Properties on Radiative Fluxes and Model Climate

In section 3 we presented results of our simulations in which the interactive dust aerosols were radiatively coupled to the GEOS-5 AGCM. Our simulations were evaluated against various observational aerosol data sets and compared broadly to the results from similar modeling studies. We found that the results presented here are similar in terms of aerosol emissions, burden, and residence time to simulations evaluated by AeroCom [Huneus *et al.*, 2011] and our own previous studies [Colarco *et al.*, 2010]. Our results were as well consistent with observations of AOT from AERONET, MODIS, and MISR, and vertical profiles observed with CALIOP. Significantly, we found that summertime Saharan dust was transported over longer distances, at higher altitude, and more northward in simulations with relatively higher aerosol absorption (OPAC and SF optical models) than in simulations with less or no absorption (OBS optical model and No Forcing).

Table 5. Global, Annual Mean (2041–2050) All-Sky Dust Aerosol Radiative Effect [W m^{-2}] for Our Different Optical Lookup Tables

	SW TOA	SW ATM	SW SFC	LW TOA	LW ATM	LW SFC	TOT ATM
OPAC-Spheres	−0.16	1.43	−1.59	0.13	−0.57	0.70	0.86
OPAC-Spheroids	−0.15 (−6%)	1.71 (20%)	−1.86 (17%)	0.11 (−10%)	−0.52 (−8%)	0.64 (−8%)	1.18 (38%)
OPAC-Ellipsoids	−0.18 (9%)	1.54 (8%)	−1.72 (8%)	0.11 (−9%)	−0.53 (−7%)	0.65 (−7%)	1.01 (17%)
SF-Spheres	0.05	1.69	−1.64	0.05	−0.27	0.33	1.42
SF-Ellipsoids	0.04 (−31%)	1.77 (5%)	−1.74 (6%)	0.05 (−9%)	−0.25 (−8%)	0.30 (−8%)	1.52 (7%)
OBS-Spheres	−0.35	0.77	−1.11	0.05	−0.27	0.32	0.49
OBS-Spheroids	−0.32 (−7%)	0.92 (21%)	−1.25 (12%)	0.05 (−9%)	−0.25 (−8%)	0.30 (−8%)	0.67 (36%)

^aPercent differences relative to the relevant spheres case (i.e., grouped by refractive index) are shown in parentheses. Calculations are based on the atmospheric state, surface reflectivity, and dust distributions from the OPAC-Spheres model run.

Here we assess the impact of the dust spatial distribution and optical properties on the radiative fluxes calculated in the GEOS-5 model, and the impact on these fluxes on the model climate.

4.1. Impact of Dust Particle Shape on Diagnosed Radiative Fluxes

In order to unravel the impact of dust particle shape from the dust spatial distribution, we performed a series of diagnostic calculations using a prescribed atmospheric state (clouds, temperature, etc.), surface reflectivity, and dust mass and particle size distribution drawn from the last ten years of our OPAC-Spheroids model run. All-sky shortwave and longwave radiative fluxes were calculated hourly with the time-appropriate fields using an offline version of the GEOS-5 radiative transfer module. Our calculation follows the presentation in *Randles et al.* [2013] and is shown as the net (positive down) flux change with and without aerosols, holding the atmospheric state fixed between two separate calls to the radiative transfer module. Defined this way, a positive top-of-atmosphere (TOA) forcing indicates the addition of energy to the climate system (i.e., a radiative warming effect), while a negative forcing indicates a net energy loss (i.e., a radiative cooling effect). Calculations are performed for each of our lookup tables of dust optical properties. The radiative impact of sea-salt aerosols has been removed in these calculations.

Table 5 summarizes the climatology of the globally, annually averaged all-sky dust radiative fluxes computed for each of the optical models using atmospheric state and dust fields from the last ten years (2041–2050) of the OPAC-Spheres model run. Also shown is the percent difference of the climatological value of OPAC-Spheroids and OPAC-Ellipsoids calculations, respectively, versus the spherical model baseline, grouped for each refractive index set (i.e., OPAC-based simulations compared to OPAC-Spheres, SF-Ellipsoids compared to SF-Spheres). For the OPAC-based tables, we find a shape effect on the TOA shortwave fluxes of −5% for the OPAC-Spheroids optics and +8% for the OPAC-Ellipsoids optics. This can be compared with the −4% shortwave TOA effect of the spheroidal model used in *Räisänen et al.* [2012] when compared to their spherical calculations. Shape effects exert greater surface cooling for both our spheroidal (17%) and ellipsoidal models (8%), opposite of the 3% warming that was found by *Räisänen et al.* [2012]. The shortwave atmospheric forcing is 1.43 W m^{-2} for the OPAC-Spheres model, versus the much smaller 0.24 W m^{-2} inferred from *Räisänen et al.* [2012], and we find greater atmospheric forcing for our spheroidal and ellipsoidal models. Results are consistent for the SF- and OBS-based simulations, again indicating the relatively greater shortwave atmospheric forcing for spheroids than for ellipsoids. Note the large percent difference in the shortwave TOA forcing for SF-based simulations is owing to the small absolute magnitude of the signal.

An important distinction between our results and those in *Räisänen et al.* [2012] is that their refractive indices were much less absorbing in the shortwave than those in the OPAC database, which is consistent with the overall difference of our results from theirs. We find a longwave shape effect of about −10% in all flux components for both our spheroidal and ellipsoidal models. Total (shortwave + longwave) atmospheric forcing is 37% greater for the spheroidal model versus spheres, and 17% greater for the ellipsoidal model. Recall that the midvisible AOT was enhanced 25% for both the spheroidal and ellipsoidal models versus the spherical model for the same aerosol loading (Figure 2 and Table 1). This and the relatively enhanced forward scattering (asymmetry parameter in Table 1) explain this enhanced atmospheric forcing, as—if anything—the single scattering albedo is higher in the nonspherical models used than for the spherical model (Figure 2).

Table 6. Global, JJA Climatological (2041–2050) All-Sky Dust Aerosol Radiative Effect (W m^{-2})

	SW TOA	SW ATM	SW SFC	LW TOA	LW ATM	LW SFC	TOT ATM
OPAC-Spheres	−0.14	1.99	−2.13	0.21	−0.61	0.82	1.37
OPAC-Spheroids	−0.12	2.37	−2.49	0.19	−0.57	0.76	1.80
OPAC-Ellipsoids	−0.16	2.14	−2.29	0.19	−0.58	0.77	1.56
SF-Spheres	0.14	2.35	−2.21	0.09	−0.31	0.40	2.04
SF-Ellipsoids	0.13	2.46	−2.33	0.09	−0.29	0.37	2.17
OBS-Spheres	−0.41	1.07	−1.48	0.09	−0.31	0.40	0.77
OBS-Spheroids	−0.37	1.29	−1.66	0.08	−0.28	0.37	1.01

4.2. Online Radiative Fluxes for Different Dust Distributions and Optical Properties

In section 4.1 we diagnostically computed dust radiative fluxes for different assumptions of the particle shape distribution using a fixed atmospheric state and dust mass distribution from one of our simulations. Here we analyze the dust radiative fluxes computed in our individual simulations. We return our attention to the JJA time period in order to make the connection between the dust radiative fluxes and the mass distributions analyzed in section 3. Table 6 summarizes the year 2041–2050 climatological JJA global all-sky dust radiative effect in our simulations (the JJA and annual mean climatological values broken out by land and ocean are presented in Tables S4 and S5, respectively; JJA and annual clear-sky values are presented in Tables S6 and S7, respectively). Again, the sea salt radiative effect has been removed in what is presented.

Table 6 indicates a net clear-sky TOA shortwave cooling for the OPAC- and OBS-based simulations. Table S4 breaks these components into land and ocean portions, showing shortwave TOA warming over land in the OPAC- and SF-based simulations, with the warming over land much more pronounced in the SF-based simulations (hence the overall positive shortwave TOA forcing for the SF models shown in Table 6). The weak absorption in the OBS-based simulations leads to the largest shortwave TOA cooling. The total TOA effect (shortwave + longwave) is almost zero in the OPAC-based simulations, a slight warming in the SF-based simulations, and cooling in the OBS-based simulations.

Figure 15 shows the climatological, JJA all-sky shortwave TOA “forcing efficiency” (forcing per unit AOT) for several of our model runs over northern Africa and the North Atlantic Ocean. Note that we show forcing efficiency in Figure 15 to facilitate comparison of the simulations, but that absolute forcing values are shown in Tables 6 and S4–S7. So, for example, we show the forcing efficiencies for our SF-Spheres and OPAC-Spheres cases, as well as the difference between them. Also shown is the low cloud area fraction (i.e., clouds at altitudes lower in altitude than pressure > 700 hPa in the model) for each simulation. For clarity, we screen out areas where the climatological dust AOT < 0.01 . The low cloud fraction is similar for both simulations. For the SF-Spheres simulation there is positive forcing efficiency (warming) over the ocean where the low cloud fraction is greatest. We note that the SF-based simulations had the highest mean transport altitude (Figure 14), and the shortwave TOA fluxes above the clouds are consistent with an absorbing aerosol above a bright, reflective surface. Except over that peak of low cloud fraction, for both simulations there is a negative forcing efficiency over the ocean, and there is positive forcing efficiency over the dust source regions.

Also shown in Figure 15 is the shape effect, presented as the difference of the OPAC-Ellipsoids and OPAC-Spheroids models relative to the OPAC-Spheres baseline. The nonspherical optical models are relatively cooling at TOA over the source region compared to the spherical model but are somewhat less cooling over the oceans or land remote from the source regions (positive differences in Figure 15).

Finally, in Figure 15 we show the difference of the OBS-Spheres model compared to the OPAC-Spheres baseline. The OBS-Spheres model is more efficiently cooling over both land and ocean, although there is a weak relative warming feature over the westernmost portion of the dust plume which is simply an artifact of our differencing because the OBS-Spheres simulation has essentially no dust AOT in this region Figure 10(right).

The dust all-sky longwave TOA effect is warming for all simulations, as shown in Table 6. The global average warming over ocean is relatively small and similar for all simulations, in the range of 0.02 – 0.07 W m^{-2} . Over land the effect is larger and more varied, between 0.18 – 0.47 W m^{-2} . The strongest longwave effect is for the OPAC based simulations, while the SF and OBS simulations are more similar. Recall that the OBS and SF simulations used the same refractive indices in the longwave. Figure 2 shows the relatively higher longwave

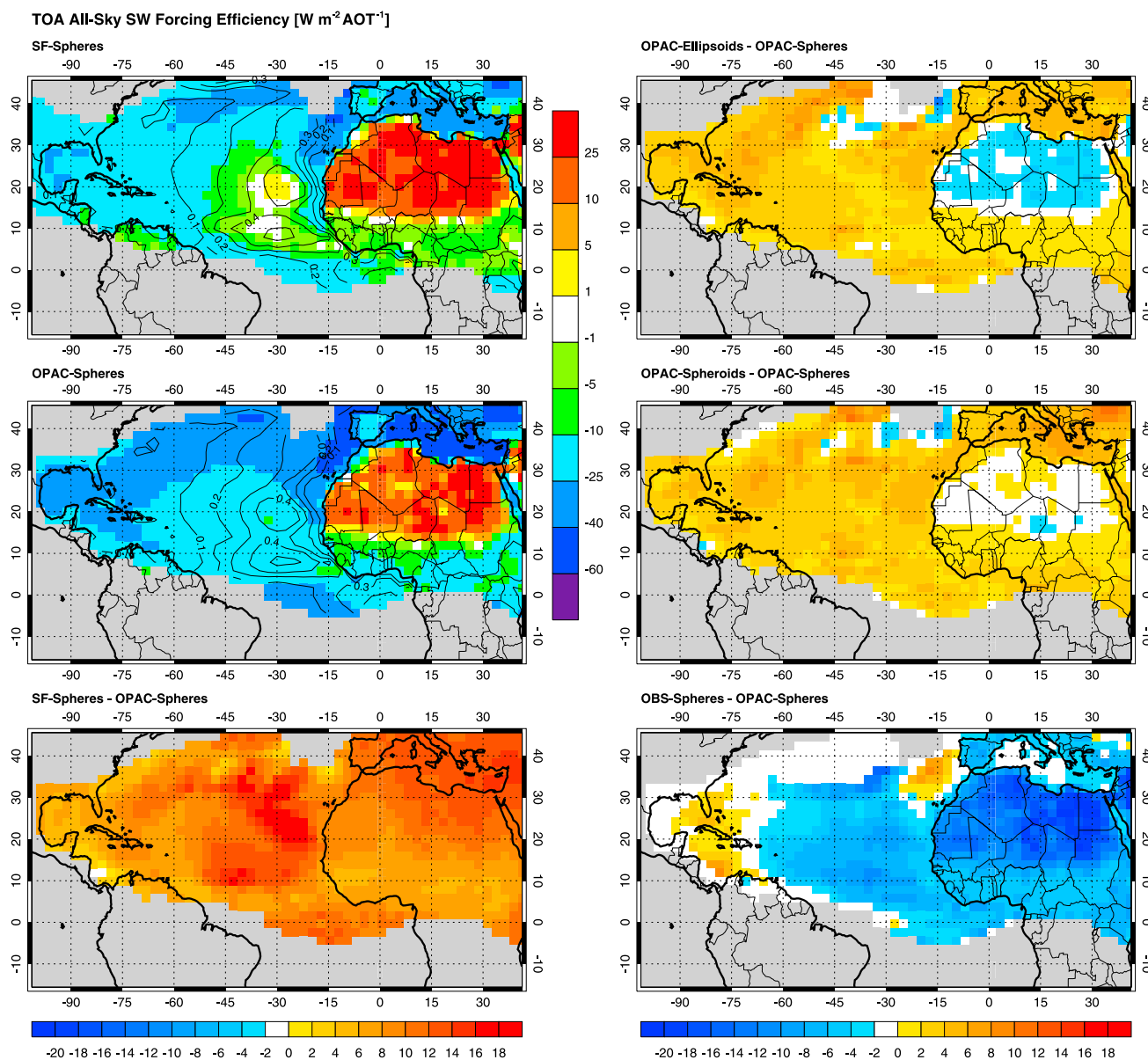


Figure 15. JJA climatology of TOA all-sky shortwave dust aerosol forcing efficiency. (left) We show the SF-Spheres and OPAC-Spheres values, as well as their difference. Contour lines indicate low cloud ($p > 700$ hPa) area fraction. (right) We show the difference only for the OPAC-Ellipsoids, OPAC-Spheroids, and OBS-Spheres simulations relative to the OPAC-Spheres baseline.

AOT and lower single scattering albedo for the OPAC refractive indices compared to the other simulations, hence the stronger longwave effect.

Surface effects are consistent among the simulations, with an overall cooling in the shortwave and warming in the longwave, and a greater magnitude for both over land than ocean. Again, the OPAC-based simulations have the greatest longwave warming.

The atmospheric forcing is the difference between the TOA and surface terms in Table 6 and is the amount of energy added or subtracted from the atmosphere due to the dust radiative effects. All of our simulations have a total (shortwave + longwave) atmospheric warming (positive forcing), driven by the balance between warming in the shortwave and relatively weak cooling in the longwave. The distinction between the different refractive index sets becomes clear, with the OBS simulations having the lowest total atmospheric forcing ($0.77\text{--}1.01\text{ W m}^{-2}$). The OPAC total forcing is intermediate ($1.37\text{--}1.80\text{ W m}^{-2}$). The SF simulations had the greatest atmospheric forcing ($2.04\text{--}2.17\text{ W m}^{-2}$), owing to their stronger shortwave warming and weaker longwave atmospheric cooling.

Differences in the direct radiative effect among the simulations due to particle shape are not clear in the longwave, although there is some consistency among them in the shortwave. The nonspherical simulations have relatively stronger shortwave surface cooling and atmospheric warming than the associated spherical simulations, and are generally more cooling over ocean (except for the OBS-Spheroids case). Fractional differences from the spherical models are more pronounced for the spheroidal than ellipsoidal cases.

4.3. Dynamical Impact of Dust Heating

The radiative forcing of dust feeds back onto the dynamics of the GEOS-5 model. An obvious feedback is on the cycle of dust mobilization itself. For example, as Figure 3 and Table 2 illustrate, there is an impact of the dust optical properties on both the magnitude and interannual variability in dust emissions. Emissions were found to be on average lowest for the No Forcing simulation and then increasing in magnitude for the OBS, SF, and then OPAC based simulations. This result is in contrast to previous studies that found decreasing dust emissions for more absorbing dust aerosols [e.g., *Perlwitz et al.*, 2001; *Miller et al.*, 2004a]. The emissions magnitude was more related to the refractive index choice than particle shape, a grouping made clearer in the total atmospheric forcing column of Table 6. Dust atmospheric forcing is highest for the SF simulations and lowest for the OBS simulations, with OPAC slightly less than the SF simulations.

Figure 16 shows the JJA climatological difference in the mean and variance of the surface winds between the OPAC-Spheres and No Forcing model runs, as well as for the OBS-Spheres and No Forcing model runs. Also shown is the *Ginoux et al.* [2001] based source function used for dust emissions, to give a sense of how changes in the wind speed correspond to dust source regions. The general pattern is for an enhancement in the climatological mean wind field near the southern edge of the Sahara for the simulations that include dust radiative forcing relative to the No Forcing simulation. The band of higher mean wind speed extends across the western half of the continent between about 15–20°N, and is partially offset by relatively weaker winds in the dust forcing simulations to the north. The wind vectors shown in Figure 16 indicate this enhanced wind speed across the southern Sahara is generally an onshore flow pattern, resulting from enhanced heating over land due to dust relative to the fixed (cooler) sea surface temperature immediately offshore. This is consistent with the previous study of *Lau et al.* [2009].

Also shown in Figure 16 are the JJA climatological differences in dust emissions between the two simulation pairs. Emissions are the convolution of the surface wind speeds with the dust source function (the thin contours in Figure 16, see also equation (1)). The region of enhanced surface winds is correlated with relatively enhanced dust emissions in the dust forcing simulations. This relationship is not perfect as the mean wind speeds do not tell the whole story: although the mean wind speed difference is small or even negative to the north of this band there are still generally enhanced emissions in this region, especially in the OPAC-Spheres simulation. This can be understood by examining the difference in the variance of the surface wind between the forcing and no forcing simulation pairs. Where the mean winds are reduced for the forcing simulation but the emissions are higher we find a greater variance about the mean wind in the forcing cases. Increased variance in the forcing simulations means a wider distribution of wind speeds about the mean. Because of the near cubic dependence of the emissions on the surface wind speed, emissions are dramatically enhanced by the high wind speed tail of the distribution, resulting in overall higher emissions despite the lower mean wind speed.

Figure 17 presents a complementary look at the dynamics of this system. Here we show the JJA climatological mean difference in the vertical profile of atmospheric temperature for the same two pairs of simulations. The profile is the zonal mean between 15°W and 0° longitude (the westernmost portion of the dust source region). Also shown is the difference in the zonal mean wind speed between the forcing and No Forcing simulations (thin solid and dashed contours) and the isosurface of dust concentrations exceeding $100 \mu\text{g m}^{-3}$ in dust concentration (thick contour line). For both pairs of simulations the presence of dust acts to heat the atmosphere between about 800–600 hPa altitude. Attenuation of incident shortwave radiation leads to a cooling under the dust plume, while longwave cooling at the top of the dust layer leads to a cooling between about 500–400 hPa altitude. This temperature signal is present in both pairs of simulations, although the signal has much higher amplitude in the OPAC-Spheres simulation, which has considerably greater atmospheric forcing and surface cooling than the OBS-Spheres simulation (Table 5). The modified temperature profile in the dust forcing simulations alters the zonal winds, adding a westerly component at the surface but strengthening the easterly jet aloft (by about 2.5 m s^{-1} for the OPAC simulations), with the peak increase in the easterly winds at about 550 hPa altitude on the southern side of the dust plume. This result is consistent

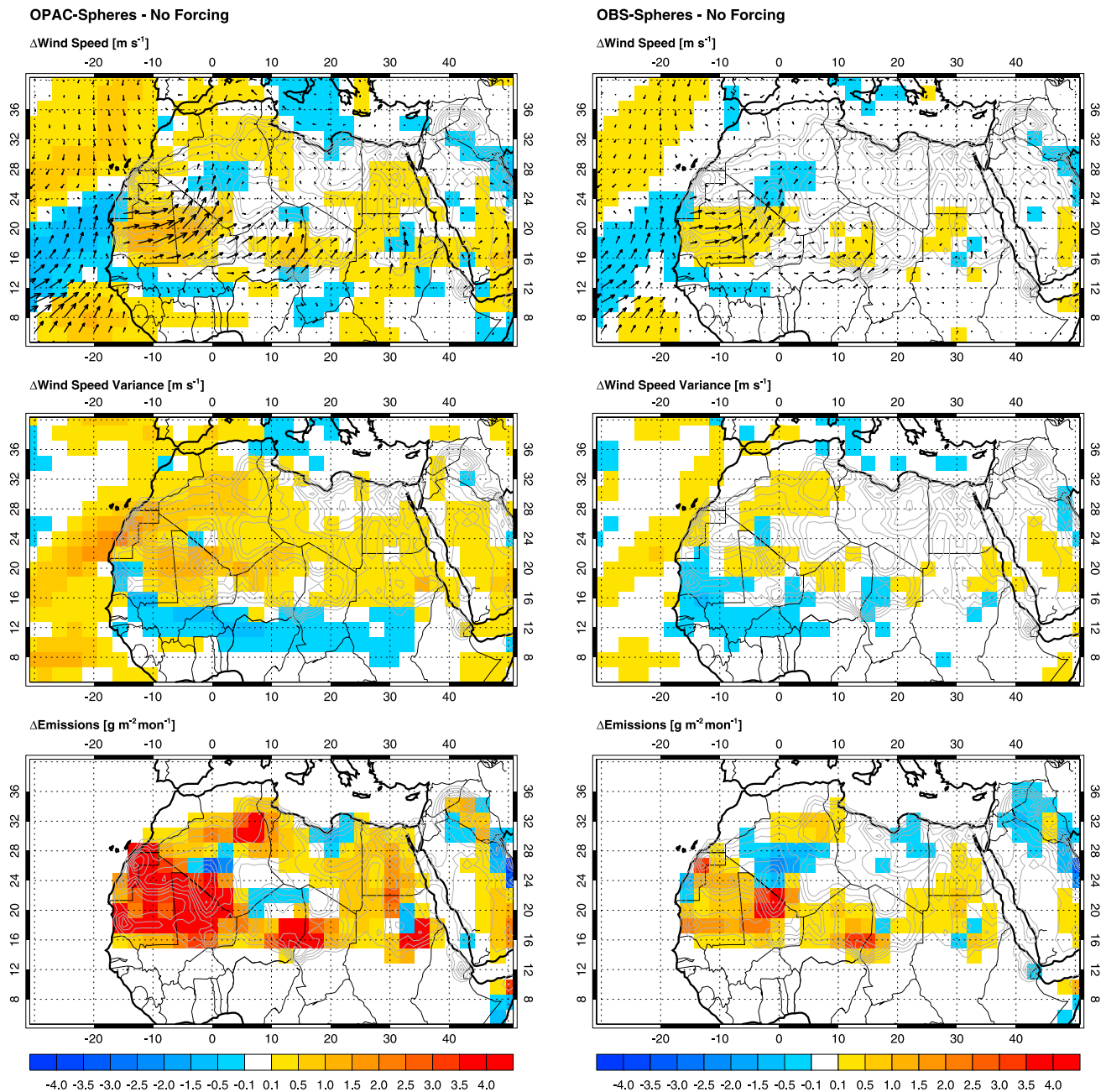


Figure 16. JJA climatology of difference in (top) mean surface wind speeds, (middle) mean variance in surface wind speeds, and (bottom) dust emissions relative to the reference No Forcing simulation. Differences are shown for the (left) OPAC-Spheres and (right) OBS-Spheres simulations. Light grey contours show the *Ginoux et al.* [2001] based source function used.

with the findings in *Kim et al.* [2010], who used a GCM with climatological aerosols to identify a strengthening of the African easterly jet south of Saharan air layer resulting from thermal wind balance with the addition of dust heating.

Figure 18 puts the dust heating effect into its global context. Here we show the JJA climatological zonal winds and mean meridional circulation (MMC) for our No Forcing simulation (contours), as well as the difference (shading) between our dust forcing simulations (again, OPAC-Spheres and OBS-Spheres) and the No Forcing model run. For the zonal mean wind, the signals seen in Figure 18 are similar to those shown for natural aerosols in *Randles et al.* [2013], who used a somewhat older version of our aerosol modeling system (their Figure 7h). For both of our dust forcing simulations shown here, there is the enhancement in the mid-tropospheric easterly wind speed in the main Saharan dust plume (between 700 and 500 hPa and 0° to 30°N,

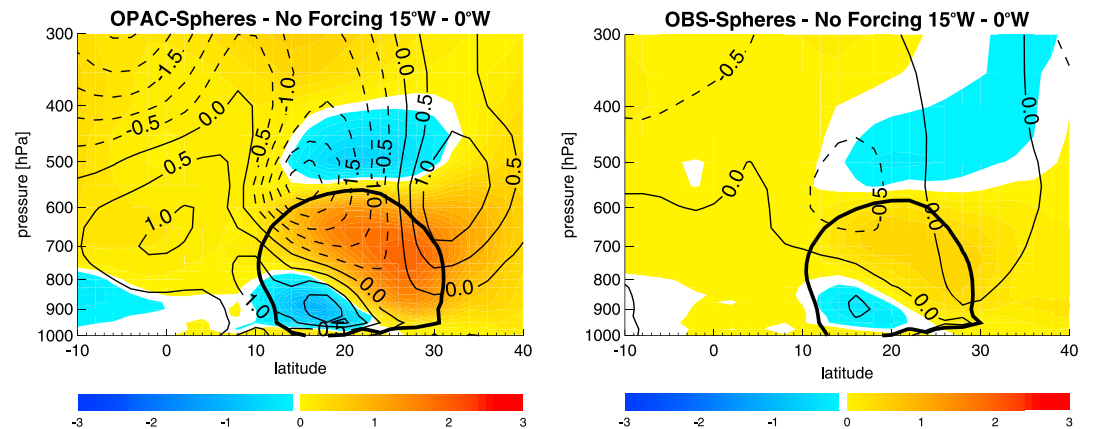


Figure 17. JJA climatology of difference in mean zonal temperature profile (shading) and zonal wind speed (thin contours) averaged 15°W–0° against the reference No Forcing simulation. The differences are for the OPAC-Spheres simulation (left) and the OBS-Spheres simulation (right). The thick contour shows the 100 $\mu\text{g m}^{-3}$ dust concentration isosurface for the perturbation experiments to indicate maximum dust concentrations.

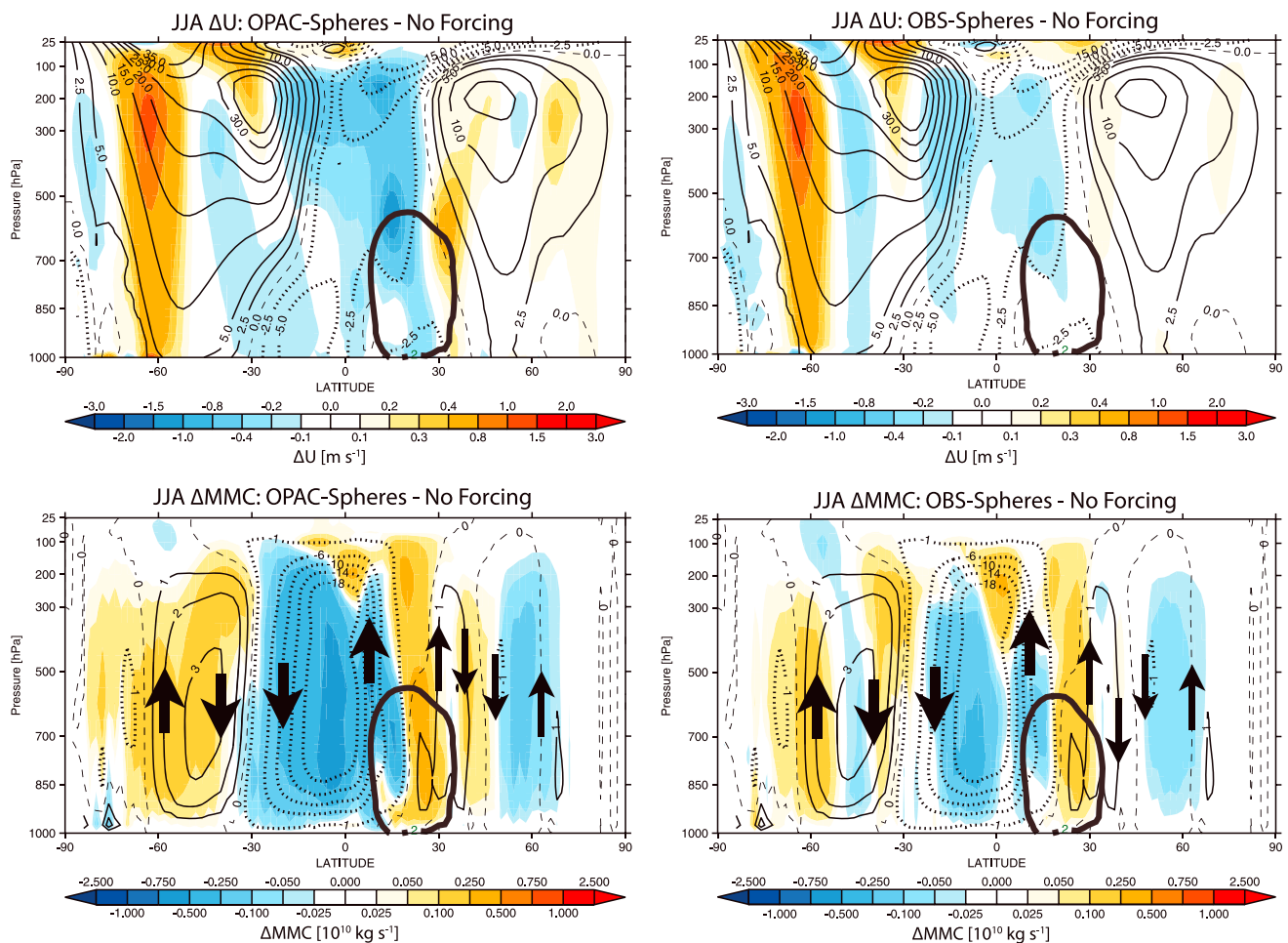


Figure 18. JJA climatology of (top) zonal averaged zonal wind and (bottom) mean meridional circulation. Contour lines show the values of the reference No Forcing simulation, while the shading shows the difference of the (left) OPAC-Spheres and (right) OBS-Spheres relative to the reference simulation. The thick contour shows the 20 $\mu\text{g m}^{-3}$ dust concentration isosurface to indicate maximum dust. The arrows give a qualitative sense of the vertical transport. For the mean meridional circulation, negative values indicate counterclockwise transport (contours) or an increase in the counterclockwise transport (shading).

similar to Figure 17). There is as well a strengthening and slight poleward shift of the southern hemisphere jet stream (at 200 hPa and 30°S). Both of these signals are stronger in magnitude in the OPAC-Spheres simulation than the OBS-Spheres. There is also an enhancement of the westerlies at about 60°S, which is similar in magnitude and structure for both pairs of our simulations. As this is a mostly dust-free environment this enhancement is likely due to the sea salt aerosols, which were very similar in all simulations (but not radiatively coupled in the No Forcing simulation). Note that the Southern Hemisphere enhancement in the westerlies is stronger in *Randles et al.* [2013], who also had a significant high bias in sea salt AOT that has largely been corrected in our model.

Figure 18 also shows the mean meridional circulation, a representation of the meridional-vertical mass stream function. The contours in Figure 18 show the sign of the MMC for the No Forcing simulation, with the arrows giving the sense and qualitative magnitude of the associated vertical motion. The effect of the aerosol forcing is to strengthen both the northern and southern branches of the Hadley cell, enhancing both the upward motion on the equatorward side of the cells and the downward motion on the poleward side. The perturbations suggest a slightly northward shift in the cell's positions, supported also by a northward shift of the ITCZ evident in the modeled precipitation fields (not shown), similar to *Wilcox et al.* [2010]. Again, the strengthening and the shift are more pronounced for the OPAC-Spheres simulation than the OBS-Spheres case. The relative enhancement of the upwelling on the equatorward side of the Hadley cell as dust absorption increases is thus the explanation for the higher dust altitude in the more absorbing dust simulations.

The results for the MMC are somewhat at odds with *Randles et al.* [2013], who diagnosed a summertime weakening of the MMC due to natural aerosols, but there are some significant differences between their simulations and ours. For one, they had a much higher baseline forcing due to high sea salt AOT (noted above). Additionally, they had annually varying SSTs, while we are using a fixed, repeating cycle of SSTs. Finally, their shortwave dust forcing was weak compared to the OPAC-Spheres model, more like what is shown in the OBS-Spheres, which has a weaker impact overall. On the other hand, the *Randles et al.* [2013] were broadly consistent with *Allen and Sherwood* [2010] who showed a similar weakening of the JJA Hadley cell due to dust and sea salt for climate model simulations with imposed (not dynamic) aerosol concentrations and fixed SSTs. Our results for the MMC, by contrast, are more like what *Randles et al.* [2013] and *Allen and Sherwood* [2010] show for anthropogenic aerosols, strengthening the Hadley cells. The anthropogenic aerosols in those studies are typically quite absorbing in the shortwave, in contrast to our OBS-Spheres simulations but more like our OPAC-Spheres model run.

5. Conclusions

We have conducted a series of experiments with the NASA GEOS-5 AGCM that incorporated a new online and radiatively coupled aerosol microphysical model. In each experiment, the lifecycles of dust and sea salt aerosols were simulated for 48 years. A climatology of sea surface temperatures was imposed, but otherwise the model climate responded to radiative forcing by the aerosols. The individual simulations differed in the assumptions of the dust optical properties, specifically, the spectral refractive index and particle shape. Differences in the dust optical properties assumed thus impact the aerosol direct radiative forcing, which in turn feeds back on the model atmosphere. We evaluated the simulated dust distributions and how they were affected by the choice of optical properties by comparing to a number of observational aerosol data sets and to results of similar dust transport models. In general, we found that our model simulated a lifecycle for dust aerosols that was similar to other dust transport models. Our model was able to capture many of the features observed for, particularly, the summertime Saharan dust plume transported over the North Atlantic Ocean. We also investigated the impact of the dust optical property assumptions on the simulated radiative fluxes and how that, in turn, affected the model climate (e.g., temperature and winds). Our results should be understood to pertain especially to Saharan dust. We recognize that dust optical properties may exhibit considerable variability depending on source region and mobilization processes, and that this may be determinant in the overall forcing of dust aerosols [*Sokolik and Toon, 1996*].

In our model, stronger dust absorption elevates the summertime Saharan plume, allowing for transport farther north and farther west. Atmospheric heating by dust aerosols and longwave cooling near the top of the plume was associated with an enhancement of the African easterly jet wind speeds, similar to what was found by *Kim et al.* [2010]. This promoted farther westward transport of the plume before it could

gravitationally settle in the simulations with the highest dust absorption. Additionally, we found that dust heating produced a strengthening and a small northward shift of the Hadley cell, similar to *Wilcox et al.* [2010], which was again more pronounced for the more absorbing dust aerosols and fostered greater dust altitude and the northward and westward transport. We found that these general features of the transport pattern were more strongly related to the choice of dust refractive index than to particle shape considerations. In other words, the radiative effects of particle shape did not significantly change the transport patterns.

We computed diagnostically and prognostically the dust shortwave and longwave radiative fluxes at the surface, in atmosphere, and at the top of atmosphere. Radiative fluxes were more clearly grouped by the choice of refractive index than by shape, consistent with our evaluation of dust transport. Shortwave surface cooling was most pronounced for the OPAC and SF simulations, while the less absorbing OBS simulations were relatively about 1 W m^{-2} less cooling. By contrast the OBS simulations were the most cooling at the TOA, followed by OPAC, and then SF, which was slightly warming at TOA. Shortwave atmospheric warming was most pronounced for SF, then OPAC, and considerably weaker for OBS. Longwave effects were similar for the OBS- and SF-based simulations, which is not surprising since the refractive indices were the same for both in the longwave. Longwave surface warming was about 0.3 W m^{-2} for the OPAC-based simulations, similar in magnitude to the difference in atmospheric cooling between OPAC and the SF- and OBS-based simulations. Total atmospheric warming was greatest for the SF-based simulations, followed by OPAC, and then OBS.

We found that higher Saharan dust emissions were associated with increased dust absorption. Table 6 shows greatest overall atmospheric heating for the SF based simulations, followed by the OPAC and the OBS based simulations. Dust emissions are similar, highest for the OPAC simulations, nearly the same for the SF runs, and lowest for the OBS and No Forcing simulations (Figure 3 and Table 2). The higher dust emissions are the result of enhancement in the surface wind speeds over important dust source regions (Figure 16).

The positive feedback of dust radiative forcing on emissions that we found is opposite to studies by *Perlwitz et al.* [2001] and *Miller et al.* [2004a], where the highest magnitude dust emissions were found for simulations in which dust was a passive tracer and the lowest overall emissions were found for the most absorbing dust optical models. Similarly, *Pérez et al.* [2006] found a strong negative feedback between dust radiative heating and emissions in a study of an intense Saharan dust event carried out in a regional model. There are important differences among these models: *Perlwitz et al.* [2001] and *Miller et al.* [2004a] were carried out in a relatively coarser spatial resolution AGCM ($4^\circ \times 5^\circ$ latitude by longitude with 12 vertical layers). The *Miller et al.* [2004a] study included a mixed-layer ocean model. In *Pérez et al.* [2006] the simulation was carried out at a 50 km horizontal spatial resolution—significantly finer than in our study—and incorporated a highly detailed representation of boundary layer dynamics. Like our study, *Pérez et al.* [2006] did not include an ocean feedback mechanism.

While inter-model differences in spatial resolution, core physics, and the inclusion an ocean feedback mechanism are doubtless part of the explanation for the different conclusion we reach about dust radiative feedback on emissions relative to prior studies, we can also assess somewhat the differences due solely to how the dust is treated in the model. For example, although *Miller et al.* [2004a] are using the same refractive indices as we are in our OPAC-Spheres model run, they arrive at a much higher single scattering albedo in the midvisible (they have 0.906, while we have 0.881 for the climatological global, annual mean). This difference is due to differences in the simulated particle size distribution. *Miller et al.* [2004b]—a companion to *Miller et al.* [2004a]—show their simulated particle size distribution of global dust loading peaks for submicron particles, while our own simulations have peak mass at supermicron sizes (e.g., see our Figure 12). This difference in the simulated particle size distribution has a significant implication for the energetics of the system. Because we have more mass at relatively larger particle sizes, we have a stronger longwave effect due to dust. There are two important aspects of this. First, our overall net dust surface radiative forcing is reduced relative to *Miller et al.* [2004a, 2004b]. While we have similar shortwave surface forcing to theirs, because of our stronger longwave heating our net forcing is -0.95 W m^{-2} (Table 5) versus -1.64 W m^{-2} reported in *Miller et al.* [2004b], and so there is a corresponding decrease in the contrast of sensible heat flux (an indication of boundary layer energetics) between our OPAC-Spheres and No Forcing runs. Second, because the net forcing in our simulations is more strongly weighted toward the longwave there is change in the diurnal cycle within the system (Figure 19). Overall net negative surface forcing peaks as expected at mid-day, but longwave effects leave a regionally strong (as much as 30 W m^{-2} in JJA seasonal climatology over the western Sahara) nighttime positive surface forcing. This enhances surface wind speeds at night relative to the day, and

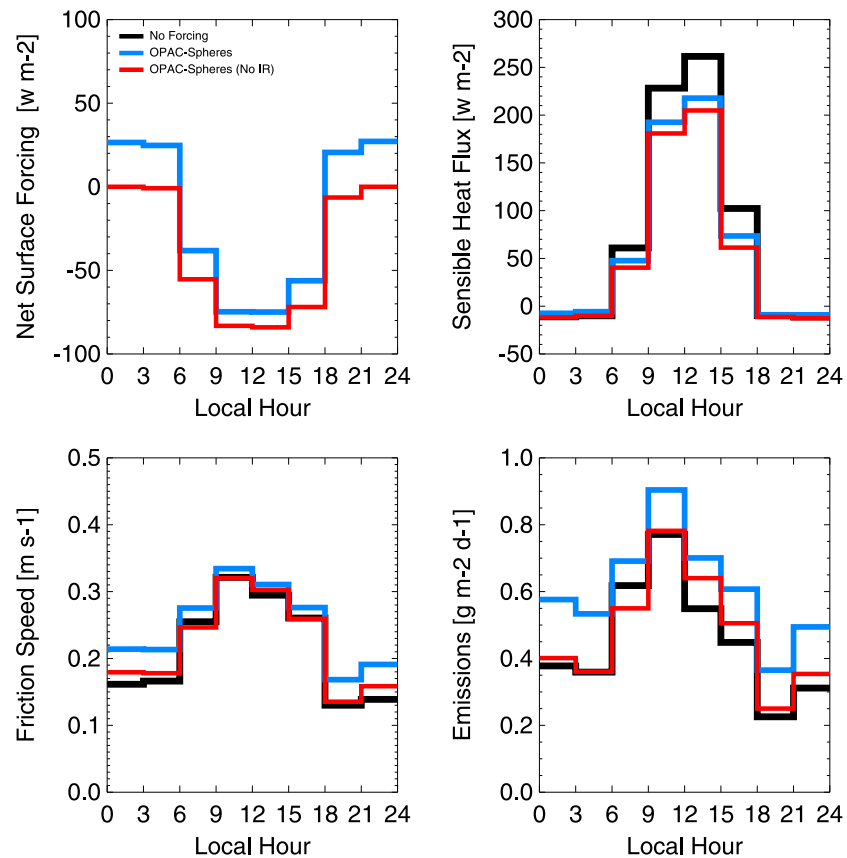


Figure 19. Diurnal, climatological JJA regionally averaged net surface forcing, sensible heat flux, friction speed, and dust emissions. Values are the regional average over the area bounded by 15°W – 5°E longitude, 16°N – 24°N latitude, the region of strongest enhancement in dust emissions over the western Sahara shown in Figure 16. Three model simulations are considered: our No Forcing case, our OPAC-Spheres case, and a simulation identical to OPAC-Spheres except that the longwave dust forcing is turned off.

there is a corresponding increase in nighttime dust emissions that largely explains the difference between our OPAC-Spheres and No Forcing model run dust emissions. This result is similar to what was found in *Stanelle et al.* [2010], who in a regional model of Saharan dust also found strong longwave forcing and a positive feedback on dust emissions. They too found an enhancement in nighttime surface winds and dust emissions. Finally, we conducted a 10 year simulation configured exactly as our OPAC-Spheres model run except that we turned off the dust longwave forcing by setting the extinction efficiency to zero in the longwave bands. This yielded a model result essentially identical to our No Forcing run in terms of diurnal cycles and overall dust emissions (Figure 19). So although turning off the dust longwave forcing did not yield the negative feedback of shortwave forcing on dust emissions that was found in previous studies, it significantly confirms the importance of dust longwave effects at least in our own simulations. We note also that in *Miller et al.* [2006] their particle size distribution was modified to be much more similar to our own, with a corresponding increase in dust longwave forcing; they did not, however, revisit the question of dust radiative feedback on emissions. *Pérez et al.* [2006] did not provide information on the simulated particle size distribution, but we note weak dust longwave forcing in their results despite simulating a very intense (midvisible AOD ~ 3.5) event. Such intense events were not studied in our coarse resolution climate model simulations presented here.

As noted above, the agreement in the simulated dust distributions with our observational data sets was better for the more absorbing SF- and OPAC-based simulations than it was for the weakly absorbing OBS-based simulations and our No Forcing model run. This result is at odds with the conclusion of remote sensing studies, which infer a less shortwave absorbing dust aerosol, more like what is used in the OBS-based simulations [e.g., *Kaufman et al.*, 2001; *Moulin et al.*, 2001; *Colarco et al.*, 2002; *Sinyuk et al.*, 2003]. One possibility is that there are important compositional changes in the aerosol (either processing of the dust by clouds or mixing with other, less absorbing aerosols) that affect the column optical properties downwind of dust

sources—where the remote sensing observations are made—but that the “pure” dust over the source region is itself relatively absorbing. If this is the case then our hypothesis is that dynamical changes to the atmosphere brought on by dust forcing are occurring over the source region. This hypothesis could be supported and we could reconcile the observationally based refractive indices of the OBS-based model runs with the desired transport features of the OPAC-based model runs if large dust particles are an important component of radiative forcing over the source region. Arguing from fundamentals of the dust emission process, Kok [2011] recommend a dust particle size distribution at emission more strongly weighted toward larger particles than we have used here and than has typically been used in dust models. Recent field observations near Saharan dust sources from the SAMUM [Weinzierl *et al.*, 2009] and Fennec [Ryder *et al.*, 2013] campaigns demonstrated the presence of a coarse dust particle mode (average volume median radius 7.75 μm for SAMUM, 11.15 μm for Fennec), for which a significant fraction of the dust mass would be neglected in our simulated particle size range that was capped at a maximum radius of 10 μm . As Ryder *et al.* [2013] makes clear, for a given refractive index for the dust, the impact of considering the full size range of particles on dust radiative properties is to reduce the single scattering albedo, which would contribute toward enhancing shortwave atmospheric heating. Though Ryder *et al.* [2013] did not consider the longwave implications of this coarse mode in their work, we suggest from our work here that further consideration of dust longwave effects would be important to understanding the energetics of dust radiative interaction with the climate system, particularly near the source regions, where such large particles would be most prominent. Far downwind those large particles would be largely removed, and the dust single scattering albedo might naturally evolve toward the values inferred in the aforementioned remote sensing studies.

Finally, it should be clear that the impact of particle shape is of secondary importance to the refractive choice as far as the transport aspects of our simulations go. Although particle nonsphericity results in a higher dust mass extinction efficiency and higher dust AOT (Table 2 and Figure 2) than for spherical properties, the character of the dust transport and emissions is most clearly grouped by refractive index choice than by particle shape (Figures 10 and 14). That said, the forcing appears to be sensitive to particle shape. As Figure 14 makes clear, the sensitivity of summertime Saharan dust median altitude over the Atlantic is such that the highest dust altitude is found in the simulation with the greatest net atmospheric forcing (all-sky, over ocean), with median altitude decreasing as atmospheric forcing decreases. Simulations with nonspherical dust optics have a higher median altitude than simulations with spherical optics but the same refractive indices. Globally, though, TOA effects are small: we found, for example, a 5% warming effect in the shortwave TOA all-sky forcing for our OPAC-Spheroids simulations relative to the OPAC-Spheres case. This result is consistent with the findings in Räisänen *et al.* [2012]. On the other hand, the ellipsoidal shape distribution resulted in an 8% cooling in the shortwave TOA with respect to OPAC-Spheres. Surface shortwave cooling was enhanced for the OPAC-Spheroids (17%) and OPAC-Ellipsoids (8%) calculations relative to spheres, at odds with the 3% warming due to spheroids found by Räisänen *et al.* [2012]. Additionally, our shortwave atmospheric warming was significantly greater than they found. When looking across the refractive index sets chosen we find consistency among them, with nonsphericity resulting in more shortwave warming than was found for spheres, enhanced relatively more for spheroids than ellipsoids, and a corresponding enhancement of surface cooling due to nonsphericity, again more pronounced for spheroids than for ellipsoids. An important distinction between our model results and theirs is that even in our least absorbing OBS-based simulations the dust absorption in our model was considerably higher than in theirs. So, although the impact of shape is similarly small in the shortwave TOA forcing—as was found in Räisänen *et al.* [2012]—we find relatively stronger impact on the atmospheric and surface forcing. The shape effect across the longwave had about 10% impact on the radiative forcing, importantly contributing to a relative atmospheric warming in the longwave that amplifies the shortwave warming effect of nonsphericity. Our overall conclusion regarding shape is thus that although the impact of shape on the shortwave TOA forcing is relatively small, it is perhaps larger and non-negligible for the atmospheric and surface forcing and is sensitive to the choice of spectral refractive index. This argues for additional studies with other shape distributions and refractive index data sets to more thoroughly explore this sensitivity, as well as focusing on regional analyses versus global (e.g., as in Figure 14). We stress that even if radiative effects of particle shape are relatively unimportant in the overall dust-climate interaction, as our studies here suggest, it is likely an important consideration for observation (i.e., radiance) simulation from modeled aerosol fields.

Future studies with this model would invoke several enhancements to our previous modeling capabilities. First, higher spatial resolution model runs would permit a more realistic simulation—and, hence, evaluation

—of dust from Asian sources. Second, while a coupled ocean model was not available in GEOS-5 at the time these simulations were performed, such a capability is being developed and can be applied to these same sorts of simulations to more fully explore the dust-climate feedback as a function of dust optical properties. Additionally, there is a need to evaluate model parameterizations, particularly with respect to wet loss processes in governing the east-west gradient of dust over the Atlantic. Particle nonsphericity was considered as it pertains to dust optical properties, but its impact as far as reducing particle fall speeds was not considered in this study [e.g., Colarco *et al.*, 2003; Ginoux, 2003]. Likewise we could as well investigate the importance of the wind speed PDF in governing dust emissions, as suggested elsewhere [e.g., Cakmur *et al.*, 2004; Su and Toon, 2009]. Finally, as is suggested above, it will be important to further assess the role coarse dust particles in our simulations. We found that our simulations evolved very similar particle size distributions that were insensitive to the dust optics and generally underestimated coarse mode dust mass compared to AERONET retrievals. Recent field experiments show the presence of large coarse mode dust particles near source regions, and suggest their importance as a radiative forcing agent. Our simulations here suggest an important role for longwave dust forcing in the energetics of the climate system, redistributing energy throughout the diurnal cycle and playing a role the positive feedback we find on dust emissions. Inclusion of a better representation of coarse mode dust particles, including simulating a wider particle size range, could be a path toward reconciling observationally based estimates suggesting a low imaginary index of refraction for dust with the desirable transport properties we found in our simulations that incorporated higher imaginary index of refraction values. Furthermore, it should be understood that our results here pertain especially to Saharan dust and that we will need to explore other regions separately, as the composition and hence optical properties of dust may vary quite strongly with source region.

Acknowledgments

The NASA Modeling, Analysis, and Prediction (MAP) program (David Considine, program manager) supported this work under project 08-MAP-80. Resources supporting this work were provided by the NASA High-End Computing (HEC) Program through the NASA Advanced Supercomputing (NAS) Division at Ames Research Center and the NASA Center for Climate Simulations (NCCS) at Goddard Space Flight Center under project SMD-11-2567. We thank Arlindo da Silva for assistance in implementing the CARMA model in GEOS-5.

References

- Ackerman, A., O. Toon, and P. Hobbs (1995), A model for particle microphysics, turbulent mixing, and radiative-transfer in the stratocumulus-topped marine boundary-layer and comparisons with measurements, *J. Atmos. Sci.*, 52(8), 1204–1236.
- Allen, R. J., and S. C. Sherwood (2010), The impact of natural versus anthropogenic aerosols on atmospheric circulation in the Community Atmosphere Model, *Clim. Dyn.*, 36(9–10), 1959–1978, doi:10.1007/s00382-010-0898-8.
- Arimoto, R., R. A. Duce, B. J. Ray, W. G. Ellis, J. D. Cullen, and J. T. Merrill (1995), Trace elements in the atmosphere over the North Atlantic, *J. Geophys. Res.*, 100(D1), 1199–1213.
- Balkanski, Y., M. Schulz, T. Claquin, and S. Guibert (2007), Reevaluation of mineral aerosol radiative forcings suggests a better agreement with satellite and AERONET data, *Atmos. Chem. Phys.*, 7, 81–95.
- Bauer, S., Y. Balkanski, M. Schulz, D. Hauglustaine, and F. Dentener (2004), Global modeling of heterogeneous chemistry on mineral aerosol surfaces: Influence on tropospheric ozone chemistry and comparison to observations, *J. Geophys. Res.*, 109, D02304, doi:10.1029/2003JD003868.
- Bian, H., and C. Zender (2003), Mineral dust and global tropospheric chemistry: Relative roles of photolysis and heterogeneous uptake, *J. Geophys. Res.*, 108(D21), 4672, doi:10.1029/2002JD003143.
- Bian, H., et al. (2013), Source attributions of pollution to the Western Arctic during the NASA ARCTAS field campaign, *Atmos. Chem. Phys.*, 13(9), 4707–4721, doi:10.5194/acp-13-4707-2013.
- Cakmur, R., R. Miller, and O. Torres (2004), Incorporating the effect of small-scale circulations upon dust emission in an atmospheric general circulation model, *J. Geophys. Res.*, 109, D07201, doi:10.1029/2003JD004067.
- Chou, M., and M. J. Suarez (1994), An efficient thermal infrared radiation parameterization for use in general circulation models, *Technical Report Series on Global Modeling and Data Assimilation*, 3, 1–98.
- Chou, M., and M. J. Suarez (1999), A solar radiation parameterization for atmospheric studies, *Technical Report Series on Global Modeling and Data Assimilation*, 15, 1–51.
- Chou, M., M. J. Suarez, X.-Z. Liang, and M. M. H. Yan (2001), A thermal infrared radiation parameterization for atmospheric studies, *Technical Report Series on Global Modeling and Data Assimilation*, 19, 1–68.
- Colarco, P., O. Toon, O. Torres, and P. Rasch (2002), Determining the UV imaginary index of refraction of Saharan dust particles from Total Ozone Mapping Spectrometer data using a three-dimensional model of dust transport, *J. Geophys. Res.*, 107(D16), 4289, doi:10.1029/2001JD000903.
- Colarco, P., O. Toon, and B. Holben (2003), Saharan dust transport to the Caribbean during PRIDE: 1. Influence of dust sources and removal mechanisms on the timing and magnitude of downwind aerosol optical depth events from simulations of in situ and remote sensing observations, *J. Geophys. Res.*, 108(D19), 8589, doi:10.1029/2002JD002658.
- Colarco, P., M. Schoeberl, B. Doddridge, L. Marufu, O. Torres, and E. Welton (2004), Transport of smoke from Canadian forest fires to the surface near Washington, D. C.: Injection height, entrainment, and optical properties, *J. Geophys. Res.*, 109, D06203, doi:10.1029/2003JD004248.
- Colarco, P., A. Da Silva, M. Chin, and T. Diehl (2010), Online simulations of global aerosol distributions in the NASA GEOS-4 model and comparisons to satellite and ground-based aerosol optical depth, *J. Geophys. Res.*, 115, D14207, doi:10.1029/2009JD012820.
- Dentener, F., G. Carmichael, Y. Zhang, J. Lelieveld, and P. Crutzen (1996), Role of mineral aerosol as a reactive surface in the global troposphere, *J. Geophys. Res.*, 101(D17), 22,869–22,889.
- Dubovik, O., and M. King (2000), A flexible inversion algorithm for retrieval of aerosol optical properties from Sun and sky radiance measurements, *J. Geophys. Res.*, 105(D16), 20,673–20,696.
- Dubovik, O., et al. (2006), Application of spheroid models to account for aerosol particle nonsphericity in remote sensing of desert dust, *J. Geophys. Res.*, 111, D11208, doi:10.1029/2005JD006619.

- Dunion, J., and C. Velden (2004), The impact of the Saharan air layer on Atlantic tropical cyclone activity, *Bull. Am. Meteorol. Soc.*, *85*(3), 353–365, doi:10.1175/BAMS-85-3-353.
- English, J., O. Toon, and M. Mills (2011), Microphysical simulations of new particle formation in the upper troposphere and lower stratosphere, *Atmos. Chem. Phys. Discuss.*, *11*, 12,441–12,486, doi:10.5194/acpd-11-12441-2011.
- English, J. M., O. B. Toon, and M. J. Mills (2012), Microphysical simulations of sulfur burdens from stratospheric sulfur geoengineering, *Atmos. Chem. Phys.*, *12*(10), 4775–4793, doi:10.5194/acp-12-4775-2012.
- Evan, A. T., J. Dunion, J. A. Foley, A. K. Heidinger, and C. S. Velden (2006), New evidence for a relationship between Atlantic tropical cyclone activity and African dust outbreaks, *Geophys. Res. Lett.*, *33*, L19813, doi:10.1029/2006GL026408.
- Fan, T., and O. B. Toon (2011), Modeling sea-salt aerosol in a coupled climate and sectional microphysical model: Mass, optical depth and number concentration, *Atmos. Chem. Phys.*, *11*(9), 4587–4610, doi:10.5194/acp-11-4587-2011.
- Feng, Q., P. Yang, G. W. Kattawar, C. N. Hsu, S.-C. Tsay, and I. Laszlo (2009), Effects of particle nonsphericity and radiation polarization on retrieving dust properties from MODIS observations, *J. Aerosol Sci.*, *40*(9), 776–789, doi:10.1016/j.jaerosci.2009.05.001.
- Fung, I., S. Meyn, I. Tegen, S. Doney, J. John, and J. Bishop (2000), Iron supply and demand in the upper ocean, *Global Biogeochem. Cycles*, *14*(1), 281–295.
- Gerber, H. E. (1985), Relative-humidity parameterization of the Navy Aerosol Model (NAM), NRL Report 8956, 1–16.
- Ginoux, P. (2003), Effects of nonsphericity on mineral dust modeling, *J. Geophys. Res.*, *108*(D2), 4052, doi:10.1029/2002JD002516.
- Ginoux, P., M. Chin, I. Tegen, J. Prospero, B. Holben, O. Dubovik, and S. Lin (2001), Sources and distributions of dust aerosols simulated with the GOCART model, *J. Geophys. Res.*, *106*(D17), 20,255–20,273.
- Ginoux, P., J. Prospero, O. Torres, and M. Chin (2004), Long-term simulation of global dust distribution with the GOCART model: Correlation with North Atlantic Oscillation, *Environ. Model. Software*, *19*(2), 113–128, doi:10.1016/S1364-8152(03)00114-2.
- Gong, S. (2003), A parameterization of sea-salt aerosol source function for sub- and super-micron particles, *Global Biogeochem. Cycles*, *17*(4), 1097, doi:10.1029/2003GB002079.
- Haapanala, P., P. Räisänen, M. Kahnert, and T. Nousiainen (2012), Sensitivity of the shortwave radiative effect of dust on particle shape: Comparison of spheres and spheroids, *J. Geophys. Res.*, *117*, D08201, doi:10.1029/2011JD017216.
- Hess, M., P. Koepke, and I. Schult (1998), Optical properties of aerosols and clouds: The software package OPAC, *Bull. Am. Meteorol. Soc.*, *79*(5), 831–844.
- Holben, B., et al. (1998), AERONET—A federated instrument network and data archive for aerosol characterization, *Remote Sens. Environ.*, *66*(1), 1–16.
- Huneeus, N., et al. (2011), Global dust model intercomparison in AeroCom phase I, *Atmos. Chem. Phys.*, *11*(15), 7781–7816, doi:10.5194/acp-11-7781-2011.
- Hurwitz, M. M., I. S. Song, L. D. Oman, P. A. Newman, A. M. Molod, S. M. Frith, and J. E. Nielsen (2011), Response of the Antarctic stratosphere to warm pool El Niño Events in the GEOS CCM, *Atmos. Chem. Phys.*, *11*(18), 9659–9669, doi:10.5194/acp-11-9659-2011.
- IPCC (2007), *Climate Change 2007: The Physical Science Basis. Contribution of Working Group I to the Fourth Assessment Report of the Intergovernmental Panel on Climate Change*, edited by S. Solomon et al., pp. 996, Cambridge Univ. Press, Cambridge, United Kingdom and New York, NY, USA.
- Jensen, E., O. Toon, D. Westphal, S. Kinne, and A. Heymsfield (1994), Microphysical modeling of cirrus: 1. Comparison with 1986 FIRE IFO Measurements, *J. Geophys. Res.*, *99*(D5), 10,421–10,442.
- Jickells, T., et al. (2005), Global iron connections between desert dust, ocean biogeochemistry, and climate, *Science*, *308*(5718), 67–71.
- Jones, C., N. Mahowald, and C. Luo (2004), Observational evidence of African desert dust intensification of easterly waves, *Geophys. Res. Lett.*, *31*, L17208, doi:10.1029/2004GL020107.
- Kahn, R., B. Gaitley, J. Martonchik, D. Diner, K. Crean, and B. Holben (2005), Multiangle Imaging Spectroradiometer (MISR) global aerosol optical depth validation based on 2 years of coincident Aerosol Robotic Network (AERONET) observations, *J. Geophys. Res.*, *110*, D10S04, doi:10.1029/2004JD004706.
- Kalashnikova, O., and I. Sokolik (2004), Modeling the radiative properties of nonspherical soil-derived mineral aerosols, *J. Quant. Spectrosc. Radiat. Transfer*, *87*(2), 137–166, doi:10.1016/j.jqsrt.2003.12.026.
- Kaufman, Y., D. Tanré, O. Dubovik, A. Karnieli, and L. Remer (2001), Absorption of sunlight by dust as inferred from satellite and ground-based remote sensing, *Geophys. Res. Lett.*, *28*(8), 1479–1482.
- Kim, K.-M., W. K. M. Lau, Y. C. Sud, and G. K. Walker (2010), Influence of aerosol-radiative forcings on the diurnal and seasonal cycles of rainfall over West Africa and Eastern Atlantic Ocean using GCM simulations, *Clim. Dyn.*, *35*(1), 115–126, doi:10.1007/s00382-010-0750-1.
- Kim, D., M. Chin, H. Yu, T. F. Eck, A. Sinyuk, A. Smirnov, and B. N. Holben (2011), Dust optical properties over North Africa and Arabian Peninsula derived from the AERONET dataset, *Atmos. Chem. Phys.*, *11*(20), 10,733–10,741, doi:10.5194/acp-11-10733-2011.
- Kinne, S., et al. (2003), Monthly averages of aerosol properties: A global comparison among models, satellite data, and AERONET ground data, *J. Geophys. Res.*, *108*(D20), 4634, doi:10.1029/2001JD001253.
- Kinne, S., et al. (2006), An AeroCom initial assessment—Optical properties in aerosol component modules of global models, *Atmos. Chem. Phys.*, *6*, 1815–1834.
- Kohfeld, K. E., and S. P. Harrison (2001), DIRTMAP: The geological record of dust, *Earth Sci. Rev.*, *54*(1–3), 81–114, doi:10.1016/S0012-8252(01)00042-3.
- Kok, J. F. (2011), A scaling theory for the size distribution of emitted dust aerosols suggests climate models underestimate the size of the global dust cycle, *Proc. Natl. Acad. Sci.*, *108*(3), 1016.
- Kostler, R., M. Suarez, A. Ducharme, M. Stieglitz, and P. Kumar (2000), A catchment-based approach to modeling land surface processes in a general circulation model 1. Model structure, *J. Geophys. Res.*, *105*(D20), 24,809–24,822.
- Lau, K. M., and K. M. Kim (2007), Cooling of the Atlantic by Saharan dust, *Geophys. Res. Lett.*, *34*, L23811, doi:10.1029/2007GL031538.
- Lau, K. M., K. M. Kim, Y. C. Sud, and G. K. Walker (2009), A GCM study of the response of the atmospheric water cycle of West Africa and the Atlantic to Saharan dust radiative forcing, *Ann. Geophys.*, *27*(10), 4023–4037.
- Lin, S. (2004), A “vertically Lagrangian” finite-volume dynamical core for global models, *Mon. Weather Rev.*, *132*(10), 2293–2307.
- Liu, H., D. Jacob, I. Bey, and R. Yantosca (2001), Constraints from Pb-210 and Be-7 on wet deposition and transport in a global three-dimensional chemical tracer model driven by assimilated meteorological fields, *J. Geophys. Res.*, *106*(D11), 12,109–12,128.
- Lock, A., A. Brown, M. Bush, G. Martin, and R. Smith (2000), A new boundary layer mixing scheme. Part I: Scheme description and single-column model tests, *Mon. Weather Rev.*, *128*(9), 3187–3199.
- Madry, W. L., O. B. Toon, and C. D. O'Dowd (2011), Modeled optical thickness of sea-salt aerosol, *J. Geophys. Res.*, *116*, D08211, doi:10.1029/2010JD014691.

- Mahowald, N., K. Kohfeld, M. Hansson, Y. Balkanski, S. P. Harrison, I. C. Prentice, M. Schulz, and H. Rodhe (1999), Dust sources and deposition during the last glacial maximum and current climate: A comparison of model results with paleodata from ice cores and marine sediments, *J. Geophys. Res.*, **104**(D13), 15,895–15,916.
- Mahowald, N. M., et al. (2009), Atmospheric iron deposition: Global distribution, variability, and human perturbations, *Ann. Rev. Mar. Sci.*, **1**, 245–278, doi:10.1146/annurev.marine.010908.163727.
- Marticorena, B., and G. Bergametti (1995), Modeling the atmospheric dust cycle: 1. Design of a soil-derived dust emission scheme, *J. Geophys. Res.*, **100**(D8), 16,415–16,430.
- Martin, J. H. (1990), Glacial-interglacial CO₂ change: The iron hypothesis, *Paleoceanography*, **5**(1), 1–13, doi:10.1029/PA005i001p00001.
- Matchuk, R. I., P. R. Colarco, J. A. Smith, and O. B. Toon (2007), Modeling the transport and optical properties of smoke aerosols from African savanna fires during the Southern African Regional Science Initiative campaign (SAFARI 2000), *J. Geophys. Res.*, **112**, D08203, doi:10.1029/2006JD007528.
- Matchuk, R. I., P. R. Colarco, J. A. Smith, and O. B. Toon (2008), Modeling the transport and optical properties of smoke plumes from South American biomass burning, *J. Geophys. Res.*, **113**, D07208, doi:10.1029/2007JD009005.
- Meng, Z., P. Yang, G. W. Kattawar, L. Bi, K. N. Liou, and I. Laszlo (2010), Single-scattering properties of tri-axial ellipsoidal mineral dust aerosols: A database for application to radiative transfer calculations, *J. Aerosol Sci.*, **41**(5), 501–512, doi:10.1016/j.jaerosci.2010.02.008.
- Miller, R. L., J. Perlwitz, and I. Tegen (2004a), Feedback upon dust emission by dust radiative forcing through the planetary boundary layer, *J. Geophys. Res.*, **109**, D24209, doi:10.1029/2004JD004912.
- Miller, R., I. Tegen, and J. Perlwitz (2004b), Surface radiative forcing by soil dust aerosols and the hydrologic cycle, *J. Geophys. Res.*, **109**, D04203, doi:10.1029/2003JD004085.
- Miller, R. L., et al. (2006), Mineral dust aerosols in the NASA Goddard Institute for Space Sciences ModelE atmospheric general circulation model, *J. Geophys. Res.*, **111**, D06208, doi:10.1029/2005JD005796.
- Mishchenko, M. I., and L. D. Travis (1998), Capabilities and limitations of a current FORTRAN implementation of the T-matrix method for randomly oriented rotationally symmetric scatterers, *J. Quant. Spectrosc. Radiat. Transfer*, **60**, 309–324.
- Mishchenko, M., A. Lacis, B. Carlson, and L. Travis (1995), Nonsphericity of dust-like tropospheric aerosols—Implications for aerosol remote-sensing and climate modeling, *Geophys. Res. Lett.*, **22**(9), 1077–1080.
- Moorthi, S., and M. Suarez (1992), Relaxed Arakawa-Schubert parameterization of moist convection for general-circulation models, *Mon. Weather Rev.*, **120**(6), 978–1002.
- Moulin, C., H. Gordon, V. Banzon, and R. Evans (2001), Assessment of Saharan dust absorption in the visible from SeaWiFS imagery, *J. Geophys. Res.*, **106**(D16), 18,239–18,249.
- Nowottnick, E., P. Colarco, A. da Silva, D. Hlavka, and M. McGill (2011), The fate of Saharan dust across the Atlantic and implications for a Central American dust barrier, *Atmos. Chem. Phys.*, **11**(16), 8415–8431, doi:10.5194/acp-11-8415-2011.
- Nowottnick, E., P. Colarco, R. Ferrare, G. Chen, S. Ismail, B. Anderson, and E. Browell (2010), Online simulations of mineral dust aerosol distributions: Comparisons to NAMMA observations and sensitivity to dust emission parameterization, *J. Geophys. Res.*, **115**, D03202, doi:10.1029/2009JD012692.
- Nussenzweig, H. M. (1992), *Diffraction Effects in Semiclassical Scattering*, Cambridge University, London.
- Ott, L., B. Duncan, S. Pawson, P. Colarco, M. Chin, C. Randles, T. Diehl, and E. Nielsen (2010), Influence of the 2006 Indonesian biomass burning aerosols on tropical dynamics studied with the GEOS-5 AGCM, *J. Geophys. Res.*, **115**, D14121, doi:10.1029/2009JD013181.
- Pérez, C., S. Nickovic, G. Pejanovic, J. M. Baldasano, and E. Özsoy (2006), Interactive dust-radiation modeling: A step to improve weather forecasts, *J. Geophys. Res.*, **111**, D16206, doi:10.1029/2005JD006717.
- Perlwitz, J., I. Tegen, and R. Miller (2001), Interactive soil dust aerosol model in the GISS GCM 1. Sensitivity of the soil dust cycle to radiative properties of soil dust aerosols, *J. Geophys. Res.*, **106**(D16), 18,167–18,192.
- Prospero, J. M. (1996), The atmospheric transport of particles to the ocean, in *Particle Flux in the Ocean*, edited by V. Ittekkot et al., pp. 19–52, John Wiley & Sons Ltd., New York.
- Prospero, J. (1999), Long-range transport of mineral dust in the global atmosphere: Impact of African dust on the environment of the southeastern United States, *Proc. Natl. Acad. Sci. U.S.A.*, **96**(7), 3396–3403.
- Prospero, J. M., M. Uematsu, and D. L. Savoie (1989), Mineral aerosol transport to the Pacific Ocean, in *Chemical Oceanography*, vol. 10, edited by J. P. Riley, pp. 187–218, Academic Press, New York.
- Prospero, J. M., P. Ginoux, O. Torres, S. E. Nicholson, and T. E. Gill (2002), Environmental characterization of global sources of atmospheric soil dust identified with the Nimbus 7 Total Ozone Mapping Spectrometer (TOMS) absorbing aerosol product, *Rev. Geophys.*, **40**(1), 1002, doi:10.1029/2000RG000095.
- Pruppacher, H. R., and J. D. Klett (1997), *Microphysics of Clouds and Precipitation*, Kluwer Academic Publishers, Dordrecht.
- Quijano, A., I. Sokolik, and O. Toon (2000), Radiative heating rates and direct radiative forcing by mineral dust in cloudy atmospheric conditions, *J. Geophys. Res.*, **105**(D10), 12,207–12,219.
- Räsänen, P., P. Haapanala, C. E. Chung, M. Kahnert, R. Makkonen, J. Tonttila, and T. Nousiainen (2012), Impact of dust particle non-sphericity on climate simulations, *Q. J. R. Meteorol. Soc.*, **139**, 2222–2232, doi:10.1002/qj.2084.
- Randles, C. A., P. R. Colarco, and A. Da Silva (2013), Direct and semi-direct aerosol effects in the NASA GEOS-5 AGCM: Aerosol-climate interactions due to prognostic versus prescribed aerosols, *J. Geophys. Res. Atmospheres*, **118**, 149–169, doi:10.1029/2012JD018388.
- Reale, O., K. M. Lau, and A. Da Silva (2011), Impact of an interactive aerosol on the African easterly jet in the NASA GEOS-5 global forecasting system, *Weather Forecast.*, **26**(4), 504–519, doi:10.1175/WAF-D-10-05025.1.
- Rienecker, M., et al. (2008), The GEOS-5 data assimilation system—Documentation of version 5.0.1, 5.1.0, and 5.2.0, NASA Technical Report Series on Global Modeling and Data Assimilation, **27**, 1–118.
- Rienecker, M. M., et al. (2011), MERRA: NASA's Modern-Era Retrospective Analysis for Research and Applications, *J. Clim.*, **24**(14), 3624–3648, doi:10.1175/JCLI-D-11-00015.1.
- Rosenfeld, D., Y. Rudich, and R. Lahav (2001), Desert dust suppressing precipitation: A possible desertification feedback loop, *Proc. Natl. Acad. Sci. U.S.A.*, **98**(11), 5975–5980.
- Rothman, L. S., et al. (2009), The HITRAN 2008 molecular spectroscopic database, *J. Quant. Spectrosc. Radiat. Transfer*, **110**(9–10), 533–572, doi:10.1016/j.jqsrt.2009.02.013.
- Ryder, C. L., et al. (2013), Optical properties of Saharan dust aerosol and contribution from the coarse mode as measured during the Fennec 2011 aircraft campaign, *Atmos. Chem. Phys.*, **13**(1), 303–325, doi:10.5194/acp-13-303-2013.
- Sassen, K., P. DeMott, J. Prospero, and M. Poellot (2003), Saharan dust storms and indirect aerosol effects on clouds: CRYSTAL-FACE results, *Geophys. Res. Lett.*, **30**(12), 1633, doi:10.1029/2003GL017371.
- Shettle, E. P., and R. W. Fenn (1979), Models for the aerosols of the lower atmosphere and effects of humidity variation on their optical properties, *Air Force Geophysics Laboratory Tech. Rep.*, AFGL-79-0214, pp. 94, Hanscom AFB, Massachusetts, USA.

- Shinn, E., G. Smith, J. Prospero, P. Betzer, M. Hayes, V. Garrison, and R. Barber (2000), African dust and the demise of Caribbean coral reefs, *Geophys. Res. Lett.*, *27*(19), 3029–3032.
- Sinyuk, A., O. Torres, and O. Dubovik (2003), Combined use of satellite and surface observations to infer the imaginary part of refractive index of Saharan dust, *Geophys. Res. Lett.*, *30*(2), 1081, doi:10.1029/2002GL016189.
- Sokolik, I., and O. Toon (1996), Direct radiative forcing by anthropogenic airborne mineral aerosols, *Nature*, *381*(6584), 681–683.
- Sokolik, I., and O. Toon (1999), Incorporation of mineralogical composition into models of the radiative properties of mineral aerosol from UV to IR wavelengths, *J. Geophys. Res.*, *104*(D8), 9423–9444.
- Stanelle, T., B. Vogel, H. Vogel, D. Bäumer, and C. Kottmeier (2010), Feedback between dust particles and atmospheric processes over West Africa during dust episodes in March 2006 and June 2007, *Atmos. Chem. Phys.*, *10*(22), 10,771–10,788, doi:10.5194/acp-10-10771-2010.
- Su, L., and O. B. Toon (2009), Numerical simulations of Asian dust storms using a coupled climate-aerosol microphysical model, *J. Geophys. Res.*, *114*, D14202, doi:10.1029/2008JD010956.
- Swap, R., M. Garstang, S. Greco, R. Talbot, and P. Kallberg (1992), Saharan dust in the Amazon Basin, *Tellus Ser. B*, *44*(2), 133–149, doi:10.1034/j.1600-0889.1992.t01-1-00005.x.
- Tanré, D., Y. Kaufman, M. Herman, and S. Mattoo (1997), Remote sensing of aerosol properties over oceans using the MODIS/EOS spectral radiances, *J. Geophys. Res.*, *102*(D14), 16,971–16,988.
- Tegen, I., and I. Fung (1994), Modeling of mineral dust in the atmosphere—Sources, transport, and optical-thickness, *J. Geophys. Res.*, *99*(D11), 22,897–22,914.
- Tegen, I., and A. Lacis (1996), Modeling of particle size distribution and its influence on the radiative properties of mineral dust aerosol, *J. Geophys. Res.*, *101*(D14), 19,237–19,244.
- Tegen, I., S. Harrison, K. Kohfeld, I. Prentice, M. Coe, and M. Heimann (2002), Impact of vegetation and preferential source areas on global dust aerosol: Results from a model study, *J. Geophys. Res.*, *107*(D21), 4576, doi:10.1029/2001JD000963.
- Textor, C., et al. (2006), Analysis and quantification of the diversities of aerosol life cycles within AeroCom, *Atmos. Chem. Phys.*, *6*, 1777–1813.
- Toon, O., R. Turco, D. Westphal, R. Malone, and M. Liu (1988), A multidimensional model for aerosols—Description of computational analogs, *J. Atmos. Sci.*, *45*(15), 2123–2143.
- Weinzierl, B., A. Petzold, M. Esselborn, M. Wirth, and K. Rasp (2009), Airborne measurements of dust layer properties, particle size distribution and mixing state of Saharan dust during SAMUM 2006, *Tellus Ser. B*, *61B*, 96–117.
- Wesely, M. (1989), Parameterization of surface resistances to gaseous drop deposition in regional-scale numerical models, *Atmos. Environ.*, *23*(6), 1293–1304.
- Wilcox, E. M., K. M. Lau, and K.-M. Kim (2010), A northward shift of the North Atlantic Ocean Intertropical Convergence Zone in response to summertime Saharan dust outbreaks, *Geophys. Res. Lett.*, *37*, L04804, doi:10.1029/2009GL041774.
- Winker, D. M., et al. (2010), The CALIPSO mission: A Global 3D view of aerosols and clouds, *Bull. Am. Meteorol. Soc.*, *91*(9), 1211–1229, doi:10.1175/2010BAMS3009.1.
- Wiscombe, W. (1980), Improved Mie scattering algorithms, *Appl. Optics*, *19*(9), 1505–1509.
- Wong, S. (2005), Suppression of deep convection over the tropical North Atlantic by the Saharan Air Layer, *Geophys. Res. Lett.*, *32*, L09808, doi:10.1029/2004GL022295.
- Yang, P., and K. Liou (1996), Geometric-optics–integral-equation method for light scattering by nonspherical ice crystals, *Appl. Optics*, *35*, 6568–6584.
- Yi, B., C. N. Hsu, P. Yang, and S.-C. Tsay (2011), Radiative transfer simulation of dust-like aerosols uncertainties from particle shape and refractive index, *J. Aerosol Sci.*, *42*(10), 631–644, doi:10.1016/j.jaerosci.2011.06.008.
- Yurkin, M. A., V. P. Maltsev, and A. G. Hoekstra (2007), The discrete dipole approximation for simulation of light scattering by particles much larger than the wavelength, *J. Quant. Spectrosc. Radiat. Transfer*, *106*, 546–57.
- Zender, C., H. Bian, and D. Newman (2003), Mineral dust entrainment and deposition (DEAD) model: Description and 1990s dust climatology, *J. Geophys. Res.*, *108*(D14), 4416, doi:10.1029/2002JD002775.
- Zender, C., R. Miller, and I. Tegen (2004), Quantifying mineral dust mass budgets: Terminology, constraints, and current estimates, *Eos. Trans. AGU*, *85*(48), 509–512, doi:10.1029/2004EO480002.
- Zhu, Y., and R. Gelaro (2008), Observation sensitivity calculations using the adjoint of the gridpoint statistical interpolation (GSI) analysis system, *Mon. Weather Rev.*, *136*(1), 335–351, doi:10.1175/MWR3525.1.